Numerical Simulation of a Axial Hydro Cyclone Separator

S.J.Kegge

6th December 2000

Contents

Chapter 1

Introduction

Cyclone separators are used in various kinds of industries to separate materials of different densities. For example they are used to dry gases (fig. 1.1), to remove solid particles from fluids or gases or to separate two fluids (fig. 1.2). By creating a strong swirl, large centrifugal forces in the process mixture are generated and due to differences in density the materials will separate. One of the many fields of application is the oil production industry. In order to optimize oil production it is necessary to separate oil from the water at an early stage. The importance of an effective compact device to do so is obvious, especially on offshore production sites. In order to discharge the production water in the sea the concentration of oil must be extremely small. This quality of water cannot be accomplished by bulk separation alone. This is where the use of a cyclone separator can be useful.

There are several types of liquid-liquid cyclone separators. The conventional design has a tangential inlet (fig. 1.2) while this study will investigate an axial cylone separator. The advantages of the last type are: less turbulence, lower pressure drop and a more compact design. There has already been an extensive experimental study of an axial design and we will compare them with the data produced by this study.

The objective of this thesis is to show and discuss the results we have produced during a Computational Fluid Dynamcis (CFD) analysis of a axial cyclone separator. I have done several simulations with swirling and non-swirling pipe flows and compared them with experimental results. I have also looked at the possibillities to simulate a cyclone separator using the same software called CFX. This software is used for industrial designing and has a wide range of application. In many cases it is capable of producing data which correspond well to experimental results. However swirling flows introduce a problem of non-isotropic turbulence which is difficult to model. The conventional $\kappa - \epsilon$ turbulence model is unable to capture the non-isotropic character of the occuring turbulence. Other models including the Reynolds Stress Model have proven to produce better data. This will also be shown by comparison with experimental data.

The structure of this report is as follows. Chapter 2 will give global insight in the working of a axial cyclone separator. In chapter 3 several techniques in numerical research are listed and discussed and a validation for the use of CFD is given. Chapter 4 will discuss several turbulence models commonly used in CFD and give their shortcomings/advantages. In chapter 5 I will present the results of simulations I have done on non-swirling flows and compare them with data obtained from experiments, DNS (Direct Numerical Simulations) and LES (Large Eddy Simulations). In chapter 6 results of swirling flow simulations are presented and compared and in chapter 7 I will give the conclusions and recommendations.

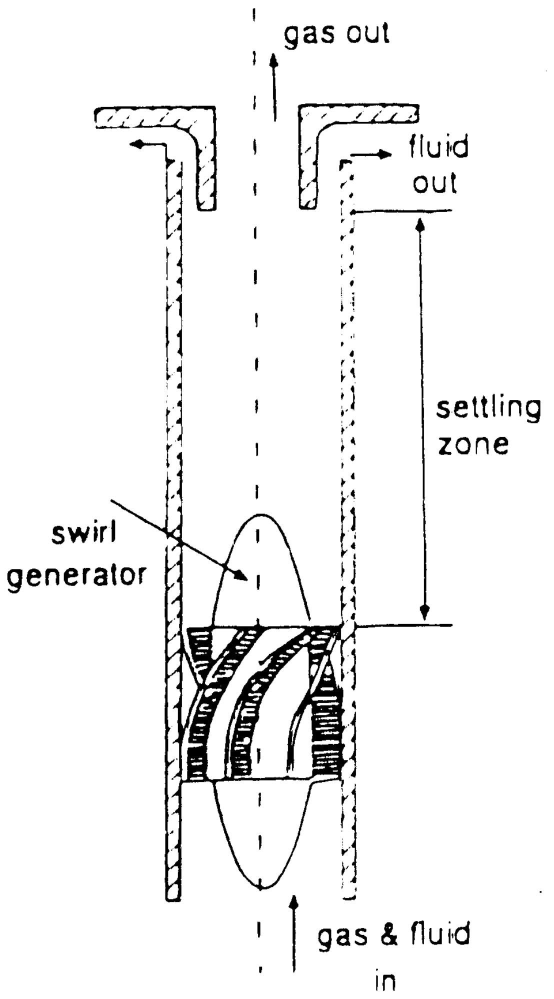

Figure 1.1: *Example of an axial cyclone separator*

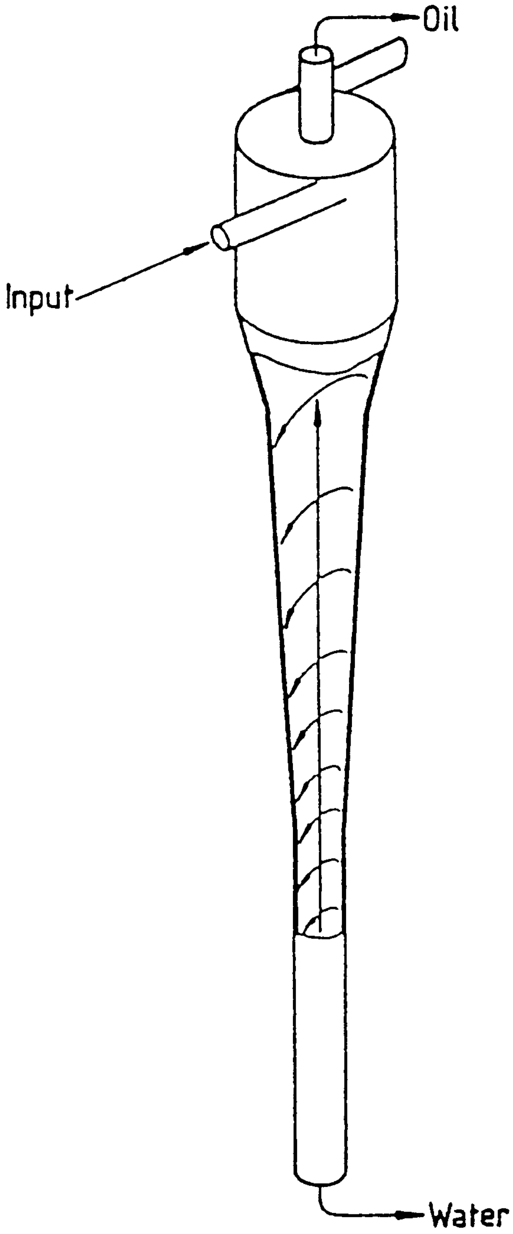

Figure 1.2: *Example of a tangential cyclone separator*

Chapter 2

Cyclone Design

In this chapter I will explain the working of the axial cyclone separator which Dirkzwager(1996) used for his experiments and which we will eventually try to simulate. The separator consists of a swirl element (see fig. 2.1) and a tube section downstream.

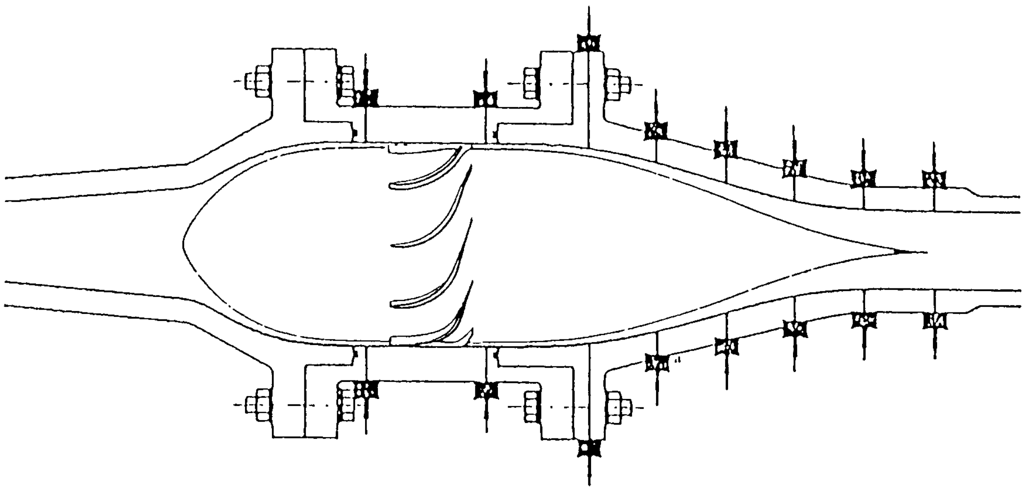

Figure 2.1: *swirlelement 72n*

The feed flow enters on the left hand side of the swirl element and the vanes on the swirl element force the flow into a centrifugal motion. After the vanes there is a converging section which increases the swirling motion of the flow. The swirl element is followed by a straight pipe where eventually the two phases will be separated.

We have gained insight in the behaviour of swirling flows by measurements done by Kitoh(1991) and Dirkzwager(1996), who did experiments on swirling flows in a straight pipe. We will use these results for comparison in chapter 6 and 7. They showed that we can expect a tangential velocity profile which is characterised by a forced vortex in the core region (solid body rotation) and a free vortex in the annular region. This is also known as Rankine's vortex (see fig. 6.5). At the wall the velocity profile shows sharp gradients due to the no-slip condition. We can also expect the peak of the tangential velocity to move towards the centreline of the pipe as the flow developes downstream. When we look at the axial velocity profiles (fig. 6.4) we see a reverse flow region.

This is caused by the negative pressure gradient which occurs when the swirl at the entrance is strong enough (For a defintion of the swirl number see chapter 6). It is caused by the wall damping of the tangential velocity which decreases the radial pressure gradient. This phenomenem is called vortex-breakdown and occurs in several cyclone seperators. Dirkzwager(1996) and Kitoh(1991) measured vortex-breakdown in their experiments.

Different types of breakdown have been observed in the past. The structure depends on the Reynolds and swirl number as vortex breakdown only occurs at high enough swirl numbers. There are two main types of breakdown:

-bubble like breakdown (axisymmetric breakdown)
-spiral like breakdown (asymmetric breakdown)

We will focus on the first type as this is the structure Kitoh(1991) and Dirkzwager(1996) observed in their experiments and what we expect to observe in our simulations (We will do axisymmetric simulations). It consists of a stagnation point and after this point there is a recirculation zone which has a bubble shape. After this zone we have a positive axial velocity. The recirculation region can be unsteady as it moves up and downstream along the centreline of the pipe. We will investigate this oscillation in our simulations in chapter 7.

A bubble type vortex breakdown is shown in figure 2.2. This is an axisymmetric simulation of a straight pipe with a narrowed section after which vortex breakdown occurs (Poppe(1999)).

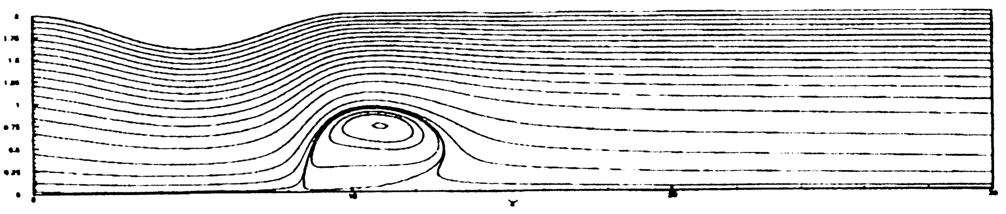

Figure 2.2: *Recirculation zone (Poppe(1999))*

Other strucures of vortex breakdown have also been observed in straight pipes. Faler and Leibovich(1978) found two recirculation cells in a slightly diverging pipe with a Reynolds number $Re = 2560$ and a swirl number of $\Omega = 1.777$.

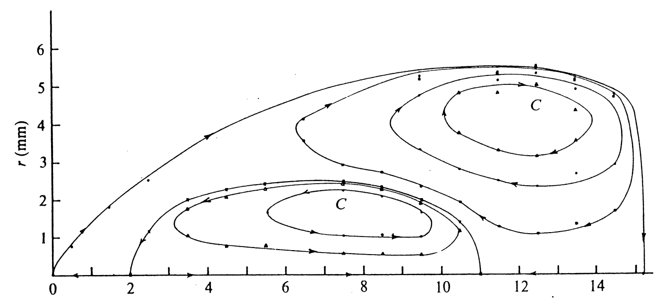

Figure 2.3: *Recirculation zone with two cells (Faler and Leibovich(1978)). Scaling on the horizontal axis is in mm.*

The final design for the separator proposed by Dirkzwager(1996) is shown in figure **??**. Due to the centrifugal forces and the difference in density between oil and water the oil will concentrate in the core region of the pipe and will be captured in the recirculation zone. By placing an extra tube in the centre of the swirl element (or upstream) the oil can be removed from the pipe to obtain a continous separation process. We will eventually try to reproduce the data Dirkzwager(1996) obtained. He did LDA (Laser Doppler Anemometry) measurements on the swirlelement 72n (without the oil discharge tube) and a straight pipe.

Figleib.eps4 cmRecirculation zone with two cells (Faler and Leibovich(1978)). Scaling on the hoerizontal axis is in mm.leib

Chapter 3

Numerical methods

3.1 Introduction

Isothermal Laminar and Turbulent flows with constant density can be described by a set of non-linear coupled partial differential equations which consist of the conservation of mass and conservation of momentum equation. The first is known as the continuity equation:

$$\frac{\partial u_i}{\partial x_i} = 0, \tag{3.1}$$

The second is known as the Navier-Stokes equation:

$$\frac{\partial u_i}{\partial t} + u_j \frac{\partial u_i}{\partial x_j} = -\frac{1}{\rho}\frac{\partial p}{\partial x_i} + \nu \frac{\partial^2 u_i}{\partial x_j^2}, \tag{3.2}$$

Solving these equations is in most cases very difficult if not impossible, especially for applications in which mechanical engineers are interested. For example flows around cars, in combustion chambers or cyclone separators. In the last few decades the computing power of computers has grown exponentially and it is expected that it will keep on growing. Therefore it has become increasingly interesting to investigate fluid dynamics using computers as they are very usefull in solving complex partial differential equations. Because mechanical engineers are not interested in the smallest scales of fluid flows but more in their effect on the mean flow quantities, it is often of no use to compute these smallest scales as done in Direct Numerical Simulations (DNS) or Large Eddy Simulations (LES). DNS solves the Navier Stokes-equations till the smallest scales (Kolmogorov scales) and LES does a direct simulation of the large-scale motion and models the scales smaller than the computational grid spacing. These time-dependant three-dimensional simulations are very expensive in computing time. Even with the newest supercomputers most flows are too complex to simulate using DNS or LES. Therefore the use of Reynolds-averaged Navier-Stokes equations (RANS) for modelling turbulent flows is very popular for designing purposes. Computational Fluid Dynamics Software (CFD) based on the RANS equations and turbulence models are available in commercial codes like CFX and FLUENT. This chapter will give a brief description of the various numerical techniques and a validation of the use of CFX is presented.

3.2 Direct Numerical Simulation

Direct Numerical Simulation is the numerical simulation of the exact three-dimensional, time-dependant Navier-Stokes equations. In these simulations no turbulence model is used so all the turbulence motions are computed. The length, time and velocity scales of the smallest turbulent motions are:

$$\eta = \left(\frac{\nu^3}{\epsilon}\right)^{1/4}$$

$$\tau = \left(\frac{\nu}{\epsilon}\right)^{1/2} \tag{3.3}$$

$$\upsilon = (\nu\epsilon)^{1/4}$$

These are known as the Kolmogorov scales. ν represents the kinematic viscosity and ϵ the energy dissipation. At these smallest scales of turbulent motion, the kinetic energy is converted to heat by means of viscous dissipation. Computing all the turbulent motions requires enormous amounts of CPU time so one can imagine that DNS is only done on non-complex geometrical cases and is rarely used to applications of engineering interest.
For example we consider a turbulent flow of water through a pipe with a diameter of $D = 0,1m$ and a bulk velocity of $U_b = 1m/s$. We choose water as processing fluid ($\nu \approx 10^{-6}m^2s^{-1}$). The Reynolds number based on bulk velocity of this flow is :

$$Re_b = \frac{U_b D}{\nu} = 10^5 \tag{3.4}$$

Reynolds numbers of this magnitude usually represent highly turbulent flows. To compute the smallest turbulence scales we use the Kolmogorov relation:

$$\epsilon \propto \frac{\mathcal{U}^3}{\mathcal{L}} \tag{3.5}$$

where $\mathcal{U}$ and $\mathcal{L}$ represent the length and velocity scale of the largest turbulence structures. The corresponding turbulent Reynolds number (based on the turbulent macroscales) is:

$$Re_{\mathcal{L}} = \frac{\mathcal{U}\mathcal{L}}{\nu} \tag{3.6}$$

Using $\mathcal{L} \sim \frac{1}{10}L$ and $\mathcal{U} \sim \frac{1}{15}U_b$ and eq. 3.5, we obtain a dissipation rate of $\epsilon \approx 3 \cdot 10^{-2}m^2s^{-3}$ (Here L represents the length scale corresponding to the flow geometry, so in our case $L = D$). Subsequently the smallest turbulent length scale $\eta \approx 7,6 \cdot 10^{-5}m$ and $Re_{\mathcal{L}} \approx 667$. For wall-bounded shear-driven flows we use the following relations (Eggels(1994)):

$$N_L = \frac{L}{\Delta x} \sim 10Re_{\mathcal{L}} \tag{3.7}$$

$$N_T = \frac{T}{\Delta t} \sim 50Re_{\mathcal{L}} \tag{3.8}$$

Were he assumed that the thickness of the viscous sublayer near the wall ($\sim \frac{\nu}{\mathcal{U}}$,) determines the scales of the smallest eddies. This means $\Delta x \sim \frac{\nu}{\mathcal{U}}$ for the axial grid spacing and $\Delta t \sim \frac{\nu}{\mathcal{U}^2}$ for the tangential grid spacing. So for a 3-dimensional time-dependent simulation of the pipe flow we need $N_L^3 \approx 3 \cdot 10^{11}$ gridpoints $N_T \approx 3 \cdot 10^4$ time steps. To give an indication, it is now possible to do DNS on large computers with 512^3 gridpoints. So it is clear that DNS is rarely used fo designing purposes. Information about small-scale turbulence provided by DNS can however be used to verify and improve existing turbulence models.

3.3 Large Eddy Simulation

A less expensive technique of simulating turbulent flows is Large Eddy Simulation (LES). By filtering the turbulence field only the large scales are resolved and the small scales of motion (smaller than the computational grid) are modelled using a subggrid-scaling (SGS) model. Small scale turbulence is assumed to have a universal structure while the large scales are flow dependent. To gain insight in LES we have a look at the undelying theory. First we filter the NS-equations spatially with filterlength l_f:

$$\frac{\partial \tilde{u}_i}{\partial x_i} = 0 \tag{3.9}$$

$$\frac{\partial \tilde{u}_i}{\partial t} + \tilde{u}_j \frac{\partial \tilde{u}_i}{\partial x_j} = -\frac{\partial}{\partial x_j}\left(\frac{\tilde{p}}{\rho}\delta_{ij} + \tau_{ij}\right) + \nu \frac{\partial^2 \tilde{u}_i}{\partial x_j^2} \tag{3.10}$$

Here τ_{ij} represents the SGS stress and a tilde represents the filtering operation. To close the set of equations we need an expression for the SGS stress. There are various SGS models and research is still done to improve them. The main advantage of LES above DNS is that it requires less CPU time. To give an indication we shall use the following relations (Eggels(1994))

$$N_L \approx 20 \frac{\mathcal{L}}{l_f} \tag{3.11}$$

For this example we shall use $\frac{\mathcal{L}}{l_f} = 5$ which corresponds to LES computations of shear-driven turbulent flows. So for a 3-dimensional time-dependent simulation of the pipe flow we need $N_L^3 \approx 1 \cdot 10^6$ gridpoints. This is still a considerable amount, especially when we keep in mind that LES is a time-dependent simulation.
At present LES-codes are becoming available in commercial form and are increasingly useful for engineering applications

3.4 Reynolds-averaged Navier-Stokes equations

Another technique of simulating turbulent flows is using Computational Fluid Dynamics (CFD) software based on the Reynolds-averaged Navier-Stokes (RANS) equations. To gain insight in the underlying theory we decompose the instanteneous variables in ensemble averaged and fluctuating quantities:

$$\begin{aligned} u &= \overline{u} + u' \\ p &= \overline{p} + p', \end{aligned}$$

where the overbar represents an ensemble average. This is called Reynolds decomposition. We use ensmble averaging as it satisfies the Reynolds conditions

$$\begin{aligned} \overline{f+g} &= \overline{f} + \overline{g} \\ \overline{\alpha f} &= \alpha \overline{f} \\ \overline{\tfrac{\partial f}{\partial s}} &= \tfrac{\partial \overline{f}}{\partial s} \\ \overline{\overline{f} g} &= \overline{f}\,\overline{g} \end{aligned}$$

Now we substitute eq. 3.12 in the continuity equation. For a incompressible flow we get:

$$\frac{\partial \overline{u}_i}{\partial x_i} = 0, \tag{3.12}$$

$$\frac{\partial u'_i}{\partial x_i} = 0, \tag{3.13}$$

Now by substituting eq. 3.12 in the NS-equations and then average the resulting equations we obtain the Reynolds-averaged Navier-Stokes equations (RANS).

$$\frac{\partial \overline{u}_i}{\partial t} + \frac{\partial \overline{u}_j \overline{u}_i}{\partial x_j} = -\frac{1}{\rho}\frac{\partial \overline{p}}{\partial x_i} + \nu \frac{\partial^2 \overline{u}_i}{\partial x_j^2} - \frac{\partial \overline{u'_i u'_j}}{\partial x_j} \tag{3.14}$$

Now we see the same as after the filtering procedure in the previous section; we are confronted with a closure problem. The last term of eq. 3.14, $\overline{u'_i u'_j}$, is called the turbulent Reynolds stress tensor and represents the transport of of x_i momentum in the direction of x_j (or vice-versa). To close the set of equations we need a turbulence model to determine the Reynolds stress tensor. There are various models with different complexity which I shall discuss in the next chapter.
The main advantage of using the RANS equations and turbulence models is that all the turbulent motions are modelled. A direct consequence is that there is no need for a small computational grid to capture these turbulent motions so these simulations require substantionally less CPU time. One can perform two or three-dimensional simulations as well as transient or steady-state simulations. Also RANS simulation codes are widespread available as commercial software which are often user friendly. On the other hand the accuracy of the simulations is dependent on the quality of the turbulence model that is used. SGS stress models which are used in LES, model the small scale turbulence which is considered universal and the energy content of the modelled eddie is supposed to be small relative to the energy content of the resolved eddies. This means that the quality of the model is less important. The RANS closure-models however model all the turbulence motions of which especially the large scales are highly flow dependent. Therefore one can expect model errors. This is why models often need fine-tuning for the flow which is under investigation. In early stages of designing processes CFD software can be a valuable tool to gain insight in the mean quantities of the flow.

Chapter 4

Turbulence modelling

4.1 Introduction

When simulating turbulent flows using LES or RANS equations, we need a turbulence model to describe the unknown turbulent correlation terms which have appeared into the mean flow equations. In case of LES we called them SGS-stresses τ_{ij} and in RANS-modelling we called them Reynolds stresses $\overline{u_i'u_j'}$. The problem of modelling these stresses is also known as the closure problem and many researchers are still investigating and trying to improve different closure models. One of the difficulties of modelling the turbulent stresses is that they are flow dependent, so there are different models for different kinds of flows. For instance Prandtl's mixing length model gives good results for turbulent wall flows but doesn't work on other flows. And Launder's κ - ϵ model does not work in swirling flows. These models will be discussed later on. To gain some more insight in turbulence modelling, have a look at figure 4.1

4.2 Prandtl's mixing-length model

One of the first turbulence models is called Prandtl's mixing-length model. To understand it we first we will have a look at the molecular stress tensor for Newtonian fluids:

$$\sigma_{ij} = -p\delta_{ij} + 2\mu s_{ij}, \tag{4.1}$$

where s_{ij} represents the mean rate of strain and is defined by:

$$s_{ij} = \frac{1}{2}\left(\frac{\partial u_i}{\partial x_j} + \frac{\partial u_j}{\partial x_i}\right) \tag{4.2}$$

Now we decompose the Reynolds stress tensor $-\rho\overline{u_i'u_j'}$ in the same way as in eq. 4.1. This means a decomposition in a isotropic pressure term and a deviatoric stress term:

$$-\rho\overline{u_i'u_j'} = -\frac{1}{3}\rho\overline{{u_k'}^2}\delta_{ij} + \rho\left(-\overline{u_i'u_j'} + \frac{1}{3}\overline{{u_k'}^2}\delta_{ij}\right) \tag{4.3}$$

Here δ_{ij} represents the Kronecker delta. Now we assume that the deviatoric part of the Reynolds stress tensor is proportional to the mean velocity gradients as in eq. 4.2:

$$\rho\left(-\overline{u_i'u_j'}+\frac{1}{3}\overline{u_k'}^2\delta_{ij}\right)=2\mu_t\overline{s}_{ij}=\mu_t\left(\frac{\partial\overline{u}_i}{\partial x_j}+\frac{\partial\overline{u}_j}{\partial x_i}\right), \tag{4.4}$$

where μ_t is known as the eddy-viscosity. The problem we are now faced with is how to model the eddy-viscosity as it is a function of the position in the flow and not a fluid property like the molecular viscosity μ. We use the following relation:

$$\mu_t \propto \rho\mathcal{U}\mathcal{L}, \tag{4.5}$$

which says that the turbulent viscosity is proportional to the largest scales of turbulent motion. Prandtl mixing-length model is based on this and calculates the eddy viscosity from :

$$\mu_t=\rho l_m^2\left(\left(\frac{\partial\overline{u}_i}{\partial x_j}+\frac{\partial\overline{u}_j}{\partial x_i}\right)\frac{\partial\overline{u}_i}{\partial x_j}\right)^{\frac{1}{2}} \tag{4.6}$$

Here l_m represents the mixing length and is dependent on the location in the flow. There are various ways of prescribing l_m. For a flow near a wall for instance we can use "von Kármán" :

$$l_m = ky \tag{4.7}$$

The mixing-length model is also known as a zero-equation model as it computes the turbulent viscosity directly from known quantities. This model is simple and fast in CPU-time but only suitable for non-complex flows due to the fact that it is difficult to estimate the mixing length.

4.3 One-Equation Models

The Prandtl κ - $\mathcal{L}$ model is an example of a one-equation model. It differs from the zero-equation model by obtaining the characteristic velocity scale of the largest eddies $\mathcal{U}$ through using the transport equation of κ :

$$\mathcal{U} \sim \kappa^{\frac{1}{2}} \tag{4.8}$$

This is based on the fact that the turbulent kinetic energy is dominated by the large scale turbulence. Now we can substitute eq. 4.8 in eq. 4.5 and this results in the following expression:

$$\mu_t = c_\mu'\rho\kappa^{\frac{1}{2}}l_m, \tag{4.9}$$

where c_μ' is a empirical constant and l_m is the mixing length. Contrary to the zero-equation models this model accounts for transport of $\mathcal{U}$ while the mixing length still has to be obtained with prior knowledge of the flow behaviour. This is the reason why these models only give reasonable results for non-complex flows.

4.4 Two-Equation Models

The two-equation models use two transport equations to describe the turbulence field. There is a wide range of two-equation models. Some examples are:

- Standard κ - ϵ model
- RNG κ - ϵ model
- Anisotropic κ - ϵ model
- Wilcox Low-Re κ - ω model

The κ - ϵ model uses the turbulent kinetic energy κ and the viscous dissipation rate ϵ to characterize the turbulent flow, where :

$$\kappa = \frac{1}{2}\overline{u_i'^2} \tag{4.10}$$

$$\epsilon = \frac{1}{2}\nu\left(\frac{\partial\overline{u_i'}}{\partial x_j} + \frac{\partial\overline{u_j'}}{\partial x_i}\right)^2 \tag{4.11}$$

Using dimensional analysis we can derive an expression for the turbulent viscosity which yields:

$$\mu_t = \rho c_\mu \frac{\kappa^2}{\epsilon}, \tag{4.12}$$

where c_μ represents a empirical turbulence constant and κ and ϵ are obtained from the transport equations :

$$\frac{D\kappa}{Dt} = P + \frac{\partial}{\partial x_j}\left(\frac{\mu_t}{\sigma_\kappa \rho}\frac{\partial \kappa}{\partial x_j}\right) - \epsilon, \tag{4.13}$$

$$\frac{D\epsilon}{Dt} = \frac{\partial}{\partial x_j}\left(\frac{\mu_t}{\sigma_\epsilon \rho}\frac{\partial \epsilon}{\partial x_j}\right) + \frac{\epsilon}{\kappa}\left(c_{1\epsilon}P - c_{2\epsilon}\epsilon\right) \tag{4.14}$$

where P represents generation of ϵ by shear :

$$P = -\overline{u_i' u_j'}\frac{\partial \overline{u}_i}{\partial x_j} \tag{4.15}$$

We have used several closure hyptheses to account for the unknown terms which occur in the original transport equations. This model accounts for transport effects of both $\mathcal{U}$ and l_m and therefore produces better results than the previous ones discussed. The standard κ - ϵ model is still very popular but also has a limited range of application. As the model is based on the eddy-viscosity concept, it can not account for anisotropic turbulence. This means that for flows with strong bodyforces (swirling flows for instance) we need to adapt the model or use a different one.

4.5 Anisotropic κ - ϵ Models

There are various models which are capable of modelling anisotropic turbulence. One option is using a anisotropic variant of the Prandtl mixing-length model as proposed by Pericleous and Rhodes(1986). Launder *et al.*(1977) proposed a modified $\kappa - \epsilon$ model. This model includes a curvature correction term in the transport equation for the energy-dissipation rate ϵ which is related to the dimensionless turbulent Richardson number Ri_t:

$$Ri_t = \frac{\kappa^2}{\epsilon^2}\frac{u_\theta}{r^2}\frac{\partial\left(ru_\theta\right)}{\partial r} \tag{4.16}$$

The modified tranport equation is:

$$\frac{D\epsilon}{Dt} = \frac{\partial}{\partial x_j}\left(\frac{\mu_t}{\sigma_\epsilon \rho}\frac{\partial \epsilon}{\partial x_j}\right) + \frac{\epsilon}{\kappa}\left(c_1 P - c_2\left(1 - c_3 Ri_t\right)\epsilon\right) \tag{4.17}$$

c_1, c_2 and c_3 are all empirical constants. This model can produce results which are in good agreement with experimental data for swirling flows (He, Salcudean and Gartshore(1999). Unfortunately the CFD software which we will use for our simulations (CFX4.2) do not include anisotropic κ - ϵ models as described above so we will not discuss these models any more.

4.6 Reynolds Stress Model

The Reynolds Stress Model (RSM) is also known as a second-order closure model as it moves the problem of closure to a higher order. It involves the solution of the transport equations of the six Reynolds stress components (3 normal and 3 shear stresses) as well as the equations for the three mean velocities and the dissipation equation. For the Reynolds stresses we can write :

$$\frac{D\overline{u_i'u_j'}}{Dt} = \frac{\partial\overline{u_i'u_j'}}{\partial t} + \overline{u_k}\frac{\partial\overline{u_i'u_j'}}{\partial x_k} = P_{ij} + T_{ij} + \Phi_{ij} - \epsilon_{ij} \tag{4.18}$$

$$P_{ij} = -\overline{u_i'u_k'}\frac{\partial u_j}{\partial x_k} - \overline{u_j'u_k'}\frac{\partial u_i}{\partial x_k} \tag{4.19}$$

$$T_{ij} = -\frac{\partial}{\partial x_k}\left(\frac{1}{\rho_0}\overline{p'u_j'}\delta_{ik} + \frac{1}{\rho_0}\overline{p'u_i'}\delta_{jk} + \overline{u_i'u_j'u_k'} + \nu\frac{\partial\overline{u_i'u_j'}}{\partial x_k}\right) \tag{4.20}$$

$$\Phi_{ij} = -\frac{1}{\rho_0}\overline{p'\left(\frac{\partial u_i'}{\partial x_j} + \frac{\partial u_j'}{\partial x_i}\right)} \tag{4.21}$$

$$\epsilon_{ij} = 2\nu\overline{\frac{\partial u_i'}{\partial x_k}\frac{\partial u_j'}{\partial x_k}} \tag{4.22}$$

The P_{ij} term is the generation of $\overline{u_i'u_j'}$, ϵ_{ij} the viscous destruction of $\overline{u_i'u_j'}$, Φ_{ij} is the pressure-strain term and T_{ij} is the transport term. We now need closure approximations for the pressure-strain term, the transport term and the viscous destruction term. First we close the pressure-strain term:

$$\Phi_{ij} = \Phi_{ij,1} + \Phi_{ij,2} + \Phi_{ij}^{w} \tag{4.23}$$

$$\Phi_{ij,1} = -C_1 \frac{\epsilon}{\kappa}(\overline{u_i' u_j'} - \frac{1}{3}\overline{u_k' u_k'}\delta_{ij}) \tag{4.24}$$

$$\Phi_{ij,2} = -C_2(P_{ij} - \frac{1}{3}P_{kk}\delta_{ij}) \tag{4.25}$$

The first term on the right hand side of eq. 4.23 is called the 'return to isotropy' term and is closed using Rotta(1951). The second term $\Phi_{ij,2}$ is closed with the "Isotropization of Production" model where P_{ij} represents the production term as in eq. 5.11. The third term on the right hand side of eq. 4.23, Φ_{ij}^{w}, accounts for the effects of a wall on the turbulence. It is called a wall reflection term and suppresses the fluctuating components normal to the wall and increases the streamwise components. The term consists of two different terms, which are modelled following by Gibson and Launder (1978):

$$\Phi_{ij}^{w} = \Phi_{ij,1}^{w} + \Phi_{ij,2}^{w} \tag{4.26}$$

$$\Phi_{ij,1}^{w} = C_1' f(l/n_i r_i)\frac{\epsilon}{\kappa}(\overline{u_k' u_m'}n_k n_m \delta_{ij} - \frac{3}{2}\overline{u_i' u_k'}n_k n_j - \frac{3}{2}\overline{u_k' u_j'}n_k n_i) \tag{4.27}$$

$$\Phi_{ij,2}^{w} = C_2' f(l/n_i r_i)(\Phi_{km,2}n_k n_m \delta_{ij} - \frac{3}{2}\Phi_{ik,2}n_k n_j - \frac{3}{2}\Phi_{kj,2}n_k n_i) \tag{4.28}$$

In both the pressure-strain closure and the wall reflection terms we have left out the buoyancy contributions as we are modelling an incompressible flow. The wall reflection terms have a significant contribution to the flow field which we will see later on.

The transport term is closed using:

$$\overline{u_i' u_j' u_k'} = -C_s \frac{\kappa}{\epsilon}\overline{u_k' u_m'}\frac{\partial \overline{u_i' u_j'}}{\partial x_m}, \tag{4.29}$$

and the viscous destruction:

$$\epsilon_{ij} = \frac{2}{3}\epsilon\delta_{ij} \tag{4.30}$$

This leaves us with: 3 turbulent transport equations for the Reynolds normal stresses, 3 turbulent transport equations for the Reynolds shear stresses, 3 transport equations for the mean velocities and one transport equation for the dissipation (+continuity equation+pressure!!!!!!). They form a set of 10 coupled non-linear partial differential equations. We need a lot of CPU-time to solve to solve these equations and they give many numerical problems. A simplification of the RSM is the Algebraic Stress Model (ASM) which solves the Reynolds stress equations by means of algebraic relations. Because the RSM is not based on the isotropic Boussinesq relation but solves the Reynolds stresses directly, it can capture anisotropic turbulence when it occurs.

4.7 Conclusion

As we are bounded by the possibilities of CFX4.2, I shall list the different turbulence models which CFX provides us:

- κ - ϵ model
- Low Reynolds Number κ - ϵ model
- Low Reynolds Number κ - ω model
- RNG κ - ϵ model
- Algebraic Stress Model
- Differential Stress Model (=RSM)
- Differential Flux Model

Unfortunately CFX doesn't provide an anisotropic κ - ϵ model. I shall use the standard κ - ϵ model in some simulations merely to show it's incapability to model 3-D swirling flows. In all other simulations I shall use the Reynolds stress model as we expect it to give the best results of all the above listed models.

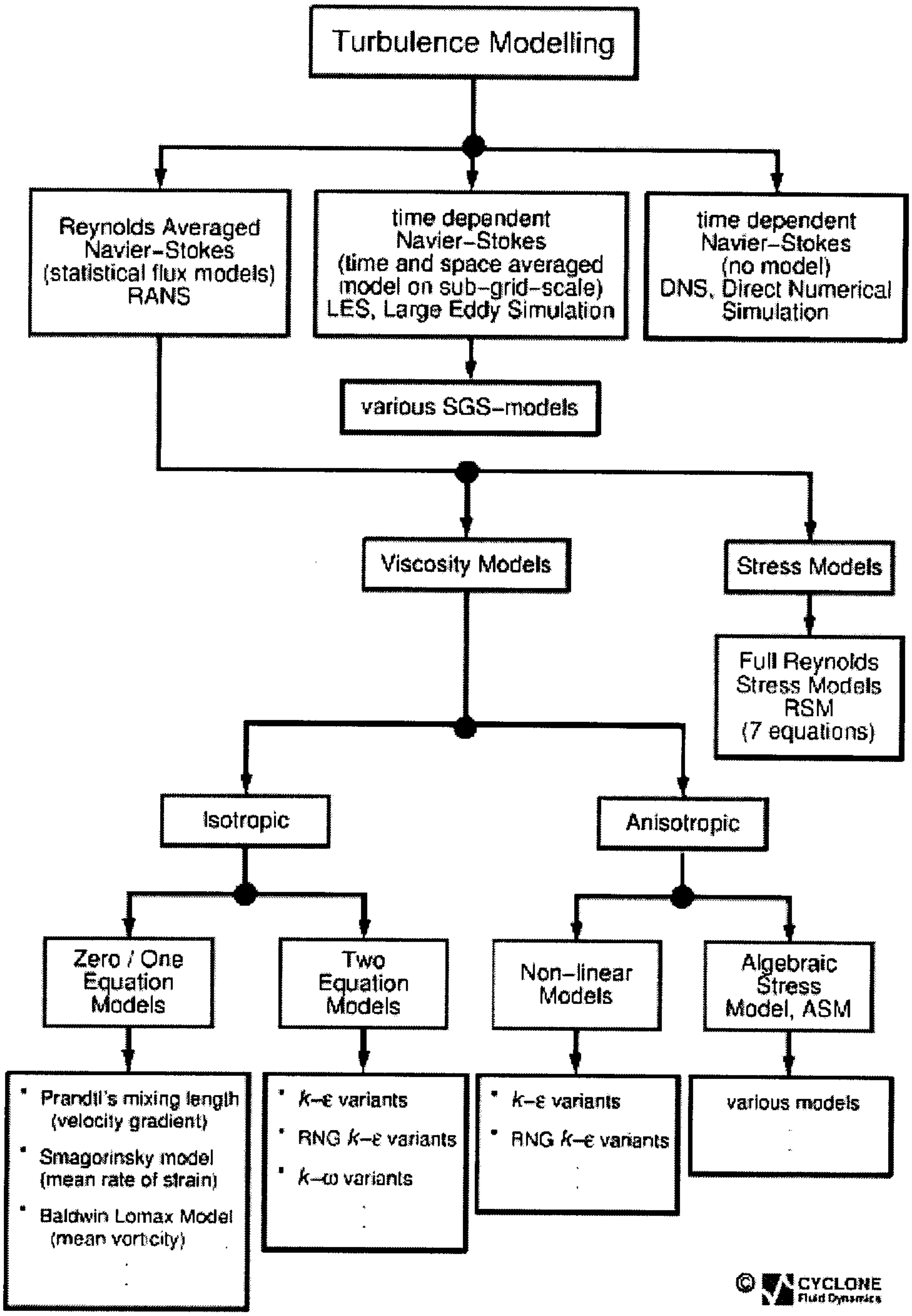

Een indeling van turbulentie modellen

Figure 4.1: *Turbulence modelling*

Chapter 5

Rotating and non-rotating pipe flows

5.1 Introduction

In order to test the performance the various turbulence models provided by CFX we start to compare numerical data produced by CFX4.2 with experimemtal data produced by Laufer(1954) and data produced by LES simulations done by Eggels(1994) for fully developed pipe flows. Eggels did LES simulations on both rotating and non-rotating flows with periodic in- and outflow boundaries. First we start with simulations on fully developed non-rotating pipe flows.

5.2 non-rotating with periodic boundary conditions

Eggels did several LES runs with different parameters and different grid spacings on a simple pipe geometry with pipe length $L_z = 5D$ and used periodic boundary conditions in $z-$ and $\theta-$ directions. One set of runs used 16 equally spaced grid points in radial direction and a wall function to bridge the near wall region (Run A to D). The other set of runs used a non-uniform gridplacing in radial direction using 32 points. In this case the first two points are located within the viscous sublayer so the equations are solved through the laminair sublayer (Run F,G,I). This means that in this case no wall function is required. As we will use a wall function we shall only compare with Run A (best results). The following parameters were used in the LES computation:

$N_r = 16, N_\theta = 64, N_z = 128,$

which represent the number of gridpoints in respectively radial, tangential and axial direction. The first runs were done to check mean velocity profiles and wall shear stress and we will use various relationships containing the wall shear stress as outlined below. For all runs the turbulent Reynolds number based on the friction velocity was:

$$Re_* = \frac{Du_*}{\nu} = 2100 \tag{5.1}$$

where,

$$u_* = \sqrt{\frac{\tau_s}{\rho}} \tag{5.2}$$

Here τ_s represents the wall shear stress and u_* the friction velocity (see Nieuwstadt(1998)). With a simple force balance we can calculate the body force required to simulate these runs :

$$\pi R^2 \Delta P = -2\pi R L \tau_s \tag{5.3}$$

When we take for $D = 1m$ and for $u_* = 1m/s$ then the mean pressure gradient is $\nabla P = 4kg/m^2s^2$. We imposed this as a body force to simulate the pipe flow. The following grid spacing was used in the simulations in CFX:

Turbulence model	$N_z \times N_r \times N_\theta$
$\kappa - \epsilon$	$3 \times 16 \times 2$
RNG $\kappa - \epsilon$	$3 \times 16 \times 2$
ASM	$3 \times 16 \times 2$
RSM	$3 \times 16 \times 2$

We used for the first runs the standard ASM and RSM models as implemented by CFX. This means that the wall reflection terms are not included and that the turbulence constants are left default.

When using 16 equally placed gridpoints in radial direction the first gridpoint is located at:

$$y^+ = y\frac{u_*}{\nu} = \frac{0.5}{16}\frac{1}{(1/2100)} \approx 32.8 \tag{5.4}$$

All the turbulence models except the Low Reynolds $\kappa - \epsilon$ model use a wall function:

$$u^+ = y^+ \quad ,\text{for } y^+ < y_0^+ \tag{5.5}$$
$$u^+ = \frac{1}{\kappa} ln(Ey^+) \quad ,\text{for } y^+ > y_0^+ \tag{5.6}$$

κ represents the von Karman constant, y_0^+ the cross-over point between the viscous sub-layer and the logarithmic region and E is a constant. The default values of κ, y_0^+ and E are respectively 0.419 , 11.23 and 9.793 (see CFX solver manual). When using a wall function the first midpoint of a gridcell y^+ next to the wall should be located in the logarithmic layer which starts at $y^+ = 30$. This is shown in fig. 5.1 where the axial velocity is plotted against the y^+ on logarithmic scale. In this first case our gridspacing in accordance with the numerical requirements.
We did a axisymmetric steady state simulation using periodic boundary conditions in $z-$ and $\theta-$ directions. The results are shown in fig. 5.2 and in fig. 5.3. We also did simulations using 32 equally placed gridpoints in radial direction (fig. **??**). In this case $y^+_{min} \approx 16.4$ thus we can expect poor results. The bulk velocities are listed in the tabel below and the axial velocity profiles in figures 5.2 and **??**.

Turbulence model	$U_b(N_r = 16)$	$U_b(N_r = 32)$
$\kappa - \epsilon$	$19.12m/s$	$18.88m/s$
RNG $\kappa - \epsilon$	$19.36m/s$	$19.21m/s$
ASM	$15.76m/s$	$15.66m/s$
RSM	$15.79m/s$	$15.69m/s$
Run A	$19.64m/s$	$*********$

The effect of placing $y^+ < 30$ is not as dramatic as the poor performance of the ASM and DSM model for this relative simple flow. The reason for this is that the standard ASM and RSM models as implemented by CFX do not include the wall reflection terms. The discrepancy for the bulk velocity is for the RSM and ASM run 25% which is rather large. The κ - ϵ and RNG κ - ϵ model

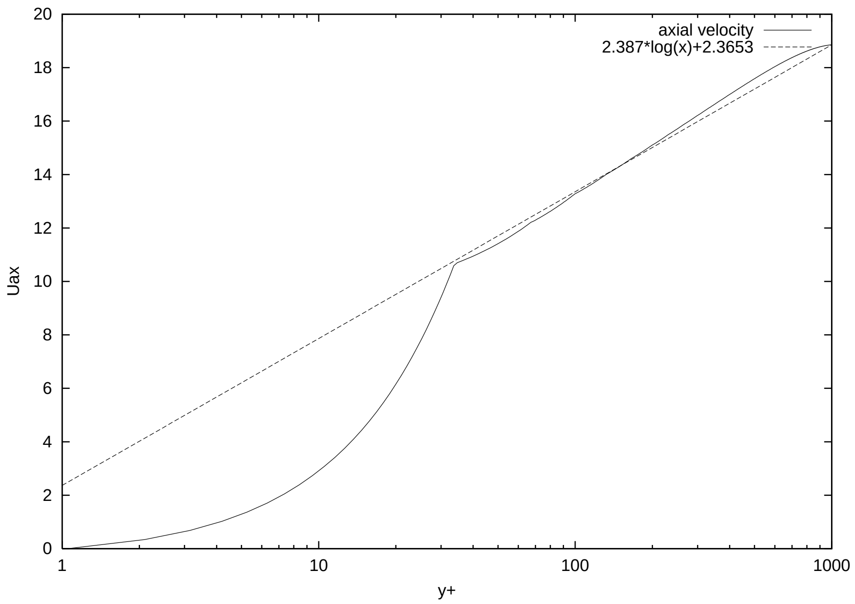

Figure 5.1: *Axial velocity as function of the distance from the wall using RSM*

perform considerably better with a discrepancy 3%. When we force a bulk velocity of $19.64m/s$ and let the flow fully develope, CFX produces a $u* \approx 1.5$ for the RSM model.

When we look at the the root-mean-square (rms) values of the velocity fluctuations (fig. 5.3) we see two things. Only the DSM and $\kappa - \epsilon$ values are shown. When using the Reynolds stress model these values are calculated directly from the transport equations. When using the $\kappa - \epsilon$ model we use the following turbulent kinetic energy equation to compute the rms values :

$$\kappa = \frac{1}{2}\overline{u_i'}^2 \tag{5.7}$$

This means:

$$u'_{z,rms} = u'_{r,rms} = u'_{\theta,rms} = \sqrt{\frac{2}{3}\kappa} \tag{5.8}$$

The $\kappa - \epsilon$ model (as expected) gives identical profiles for all three velocity fluctuations as it supposes turbulence to be isotropic and we will not discuss them any more. The RSM model does account for anisotropic turbulence but gives equal fluctuations in radial and tangential directions, see fig. 5.3(f). When we look at the experimental and LES results we see clearly a difference between the radial and tangential fluctuations as well as the axial velocity fluctuations, figures 5.3(d) and (f). The radial component is the lowest and this is because of the influence of the wall which damps the radial fluctuations and converts them to fluctuations parallel to the wall. In our runs the velocity fluctuations in radial direction are overpredicted. This seems to have a large influence on the prediction of the bulk velocity. To understand this we will have a closer look at the transport equations for the stresses:

$$\frac{D\overline{u_i'u_j'}}{Dt} = \frac{\partial\overline{u_i'u_j'}}{\partial t} + \overline{u_k}\frac{\partial\overline{u_i'u_j'}}{\partial x_k} = P_{ij} + T_{ij} + \Pi_{ij} - \epsilon_{ij} \tag{5.9}$$

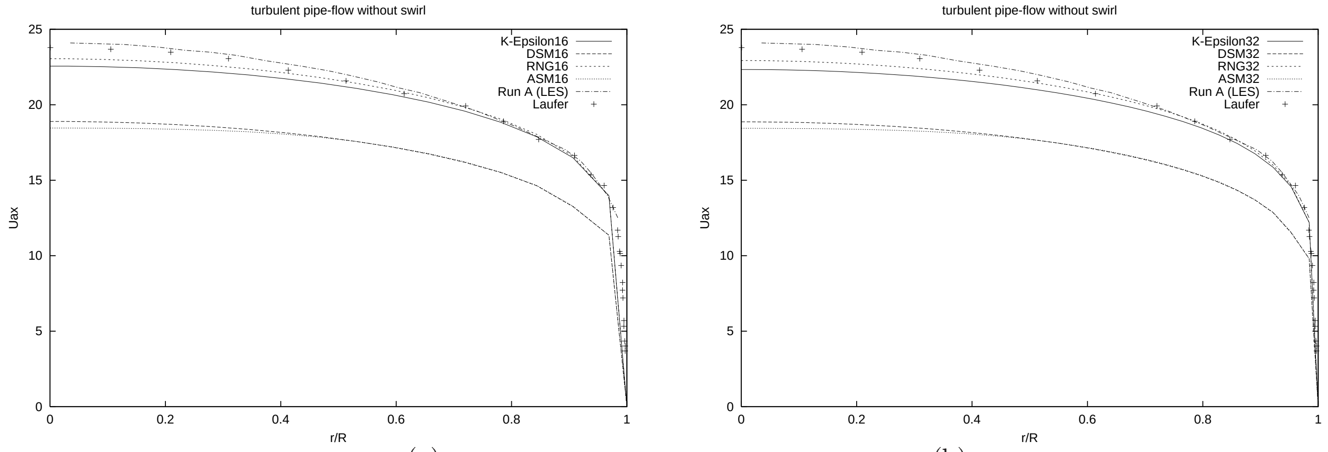

(a) (b)

Figure 5.2: *Axial velocity profile of the simulations with differently placed gridpoints*

Let us focus on the the P_{ij} term which represents the generation of $\overline{u_i'u_j'}$:

$$P_{ij} = -\overline{u_i'u_k'}\frac{\partial u_j}{\partial x_k} - \overline{u_j'u_k'}\frac{\partial u_i}{\partial x_k} \tag{5.10}$$

When using the Einstein convention and choose $i = z$ and $j = r$ we obtain the following relation,

$$P_{zr} = -\overline{u_z'u_z'}\frac{\partial u_r}{\partial z} - \overline{u_z'u_r'}\frac{\partial u_r}{\partial r} - \overline{u_z'u_\theta'}\frac{\partial u_r}{\partial \theta} - \overline{u_r'u_z'}\frac{\partial u_z}{\partial z} - \overline{u_r'u_r'}\frac{\partial u_z}{\partial r} - \overline{u_r'u_\theta'}\frac{\partial u_z}{\partial \theta} \tag{5.11}$$

The largest gradient close to the wall is the gradient of the axial velocity in radial direction. We find this gradient in the fifth term on the right hand side of eq. 5.11. So the $-\overline{u_r'u_r'}\frac{\partial u_z}{\partial x_r}$ term is dominant in the generation of $\overline{u_z'u_r'}$. In our RSM runs and ASM runs the velocity fluctuations in radial direction $\overline{u_r'u_r'}$ are overpredicted. As a direct consequence the production of shear stress is overpredicted so the mean velocity is underpredicted. This explains the large error.

To take the effect of the wall damping into account we will use wall reflection terms which damp the radial velocity fluctuations. CFX provides a user subroutine for inclusion of wall reflection terms but this routine is only apllicable in very special cases like a straight pipe flow. These terms are very complex and we have briefly discussed them in chaper 4 but for a more elaborate discussion see Gibson and Launder (1978), Wilkes and Clarke (1987) or Clarke and Wilkes (1989). The use of these extra wall reflection terms has no effect on the results produced by the $\kappa - \epsilon$. This is logical as the wall reflection terms only apply to the pressure strain term which occurs when using second order closure models (again see chapter 4). The use of these extra terms however has a large influence on the RSM results which can be seen in the tabel below and in fig. 5.4.

Run	RSM	$\kappa - \epsilon$	Run A (LES)
Re_b	47.200	40.150	41250
Re_*	2100	2100	2100
u_b/u_*	22.47	19.12	19.64
u_c/u_*	25.65	22.56	24.08
u_c/u_b	1.14	1.18	1.23

We now have a bulk velocty of $U_b \approx 22,47m/s$. Note that the error has the opposite sign of the error without wall reflection terms. When we look at the velocity fluctuations (fig. 5.5) we see the influence of the wall reflection terms in figure (d). The radial velocity fluctuations are clearly damped and the influence of this damping on the axial velocity profile is substantial.

The following conclusions can be made from these results:

- The $\kappa - \epsilon$ and the RNG $\kappa - \epsilon$ model give good results for the mean flow quantities. These models are presumably fine tuned on these flows so this is no suprise.
- The Reynolds and Algebraic stress models underestimate the mean flow quantities but do account for anisotropic turbulence. When we add wall reflection terms in the computation the behaviour of the velocity fluctuations is predicted well but we now we have an overprediction of axial velocity (see fig. 5.4).

As the Low Reynolds $\kappa - \epsilon$ model is used in the the $5000 < Re_b < 30.000$ region I will not discuss this model further as we are dealing with $Re_b > 40.000$. The RNG $\kappa - \epsilon$ model gives similar results as the standard $\kappa - \epsilon$ model so we won't discuss it anymore.

All the simulations were done using default turbulence constants which are listed below.

Turbulence constant	value	description
κ	0.4187	Von Karman constant
C_μ	0.09	Constant in eddy viscoisty formula
$C_{1\epsilon}$	1.44	Constant in ϵ-equation
$C_{2\epsilon}$	1.92	Constant in ϵ-equation
C_1	1.8	Constant in Reynolds stress equation
C_2	0.6	Constant in Reynolds stress equation
C_1'	0.5	Constant in wall reflection terms
C_2'	0.3	Constant in wall reflection terms
C_s	0.22	Constant in Reynolds stress equation
σ_κ	1.0	Turbulent Prandtl number for κ
σ_ϵ	1.375	Turbulent Prandtl number for ϵ

5.3 rotating pipe with periodic boundary conditions

Eggels(1994) also investigated the flow in a rotating pipe. He looked at fully developed swirling turbulent flow using the same pipe and the same periodic boundaries as in the previous section. To account for swirl he used a rotating pipe by imposing a tangential wall velocity of $u_{\theta,wall} = 20 \times u_*$.

$$Re_* = 2100 \tag{5.12}$$

$$Re_\theta = \frac{u_{\theta,wall} D}{\nu} = 42.000, \tag{5.13}$$

where Re_θ is the Reynolds number based on the circumferential velocity. The gridspacing is

$N_r = 16$ in the following simulations. According to CFX the Reynolds stress model will perform better when altering C_μ into 0.065 when using the wall reflection terms or altering C_μ into 0.1152 when the reflection terms are not included. C_μ is a constant used in the wall function:

$$\tau^2 = C_\mu \rho^2 \kappa^2, \tag{5.14}$$

where τ represents the wall shear stress and κ the turbulent kinetic energy (see CFX solver manual). At first glance we expect damping of the mean velocities when we increase C_μ as τ is related positively with C_μ.

To test this we performed four different runs (see tabel listed below) and compared them with experimental data taken from Reich (1988), Nishibori *et al.* (1987) and Kikuyama *et al.* (1983a) and numerical data (LES) by Eggels. We expect the ratio between the centerline velocity and the bulk velocity to be higher for the rotating pipe than for the non-rotating pipe due to the reduction of the total shear stress. The results are shown in fig. 5.6 and in fig. 5.7.

Run	Wall reflection terms	C_μ
A	no	0.09
B	yes	0.09
C	no	0.1152
D	yes	0.065

Run	Run A	Run B	Run C	Run D	$\kappa - \epsilon$	LES	Exp.
Re_b	50.900	61.400	56.400	52.630	40.150	59.500	50.000
Re_θ	42.000	42.000	42.000	42.000	42.000	42.000	50.000
$N = Re_\theta/Re_b$	0.82	0.68	0.74	0.80	0.96	0.71	1.0
Re_*	2100	2100	2100	2100	2100	2100	2000
u_b/u_*	24.37	29.24	26.87	25.06	19.12	28.31	25.4
u_c/u_*	40.81	42.89	43.43	38.36	22.56	39.18	36.1
u_c/u_b	1.67	1.47	1.62	1.53	1.18	1.38	1.42

N in the tabel above represents the ratio $N = Re_\theta/Re_b$ and u_c the centerline velocity. The $\kappa - \epsilon$ model gives the same axial velocity profile results as for the non-rotating pipe. The runs done with the Reynolds stress model do show an increase of the u_c/u_b ratio compared to the none rotating pipe flow. Run B and D appear to give the best results. The effect of altering C_μ is opposite than we expected. In Run D the mean flow quantities are damped compared to Run B where we expected the opposite behaviour. The ratio N however is increased. When we compare Run A and C we see the same behaviour.

When we look at the normalized tangential velocity profile (fig. 5.7) we see that neither of the models is able to produce good results. Experiments have shown a nearly parabolic tangential velocity profile thus we expect the same. By using the wall reflection terms the profile is slightly improved but it still is not good. Simulations done by Jakirlic(1997) with a low-Re RSM and without a wall function were able to predict the parabolic character of the tangential velocity profile (see fig. 5.8. However the figure does also show a significant error. This type of flow seems to be difficult to simulate with the Reynolds stress model.
The $\kappa - \epsilon$ model predicts solid body rotation and is clearly not able to simulate this type of flow.

5.4 Conclusions

The standard and RNG $\kappa - \epsilon$ models perform reasonably well for the non-rotating pipe flow but are not suitable for the rotating pipe flow as they do not show an increase of the ratio u_c/u_b in the

last case. Futhermore they predict a solid body rotation for the tangential velocity profile which was not measured in experiments (Reich (1988) for instance) and LES runs (Eggels(1994)).
The standard ASM and RSM models as implemented by CFX perform poorly for the non-rotating pipe flow. In order to increase the performance we have to include wall reflection terms. The mean axial velocity profile is now overpredicted but we can simulate the damping of the radial velocity fluctuations near the wall. The standard Reynolds stress model as implemented is not capable of predicting the mean flow quantities of a straight pipe flow satisfactory.
When we look at a rotating pipe flow we again see that the standard Reynolds stress model is not capable of producing good results. By including the wall reflection terms and adjusting C_μ we see a slight improvement of the tangential velocity profile but it is still different than the results produced by Jakirlic(1997) with a low-Re RSM and without a wall function. The tangential velocity profile he found did have a parabolic profile but still showed a significant error.
The other option to improve the results is leaving out the wall reflection terms and modifying C_μ into 0.1152. This option does not account for damping by the wall of the radial velocity fluctuations so the first option is the best approximation of the reality.

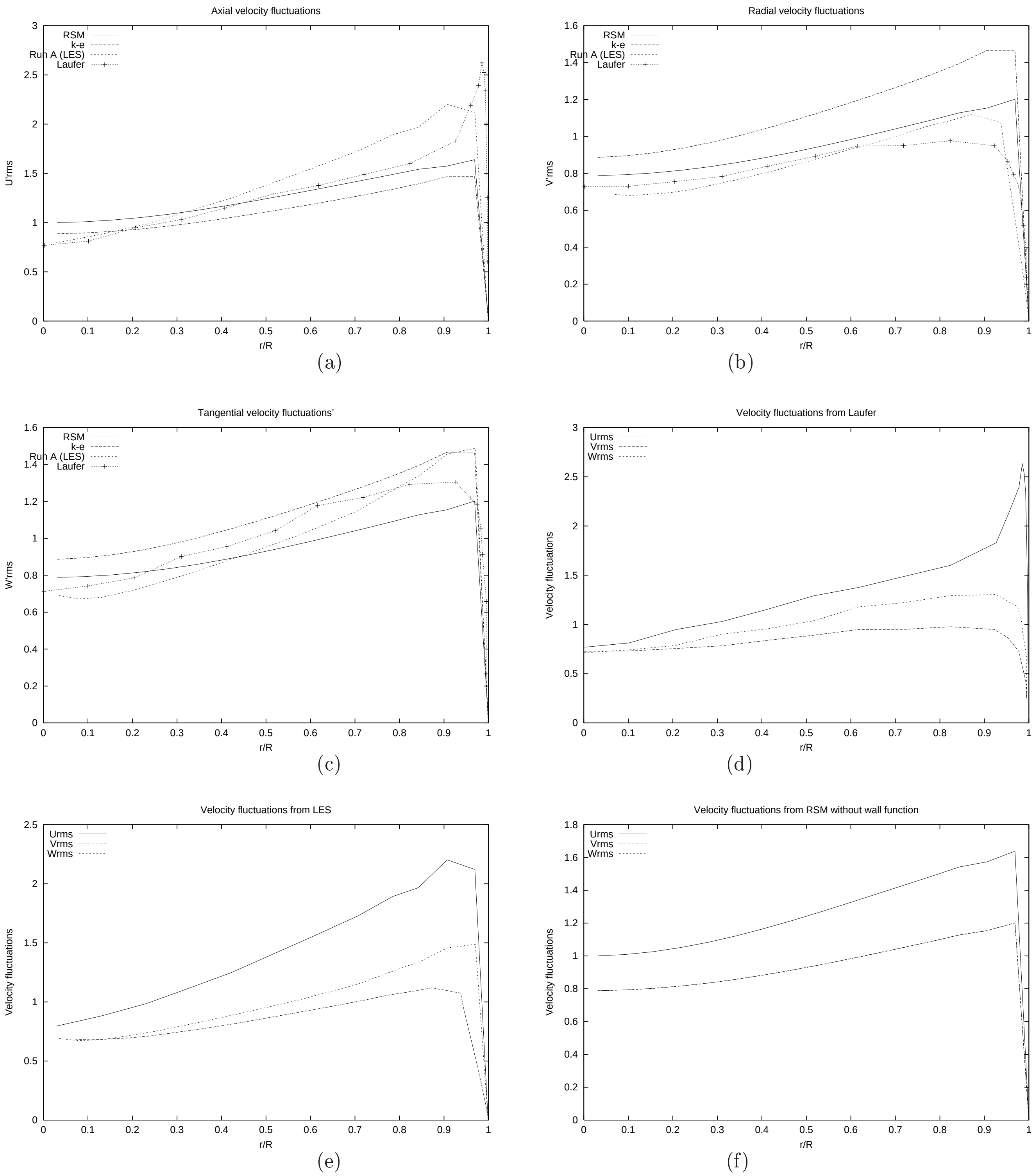

Figure 5.3: *Velocity fluctuations*

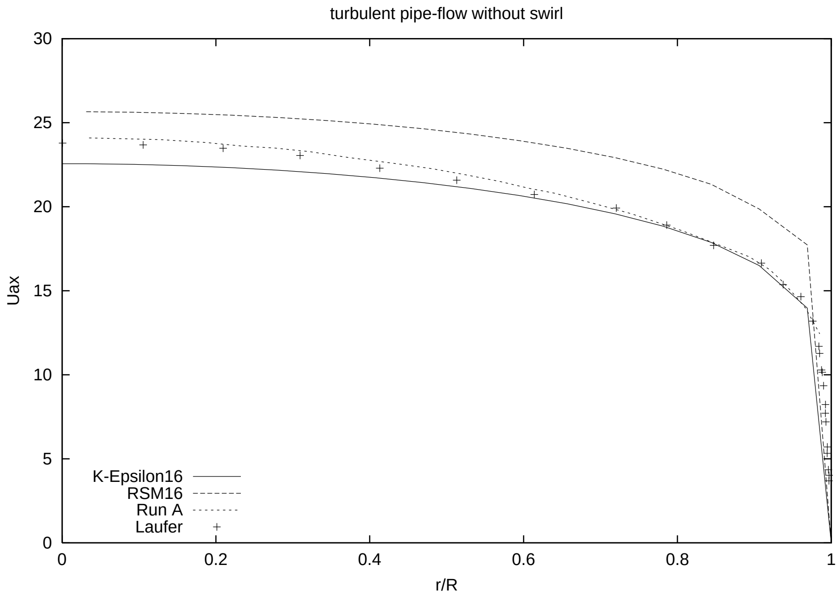

Figure 5.4: *Axial velocity profiles with RSM using wall reflection terms*

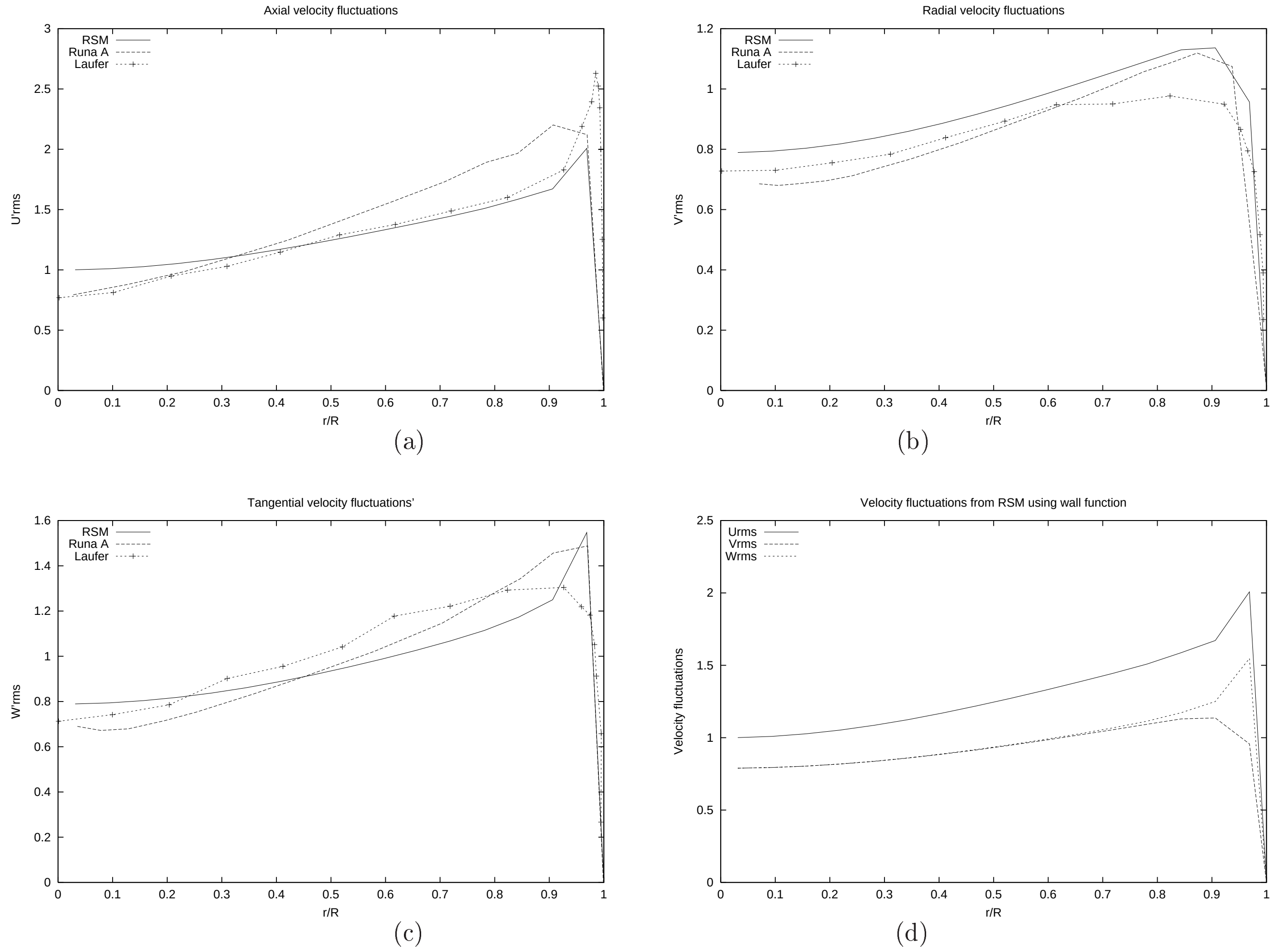

Figure 5.5: *Velocity fluctuations in axial, radial and tangential direction.*

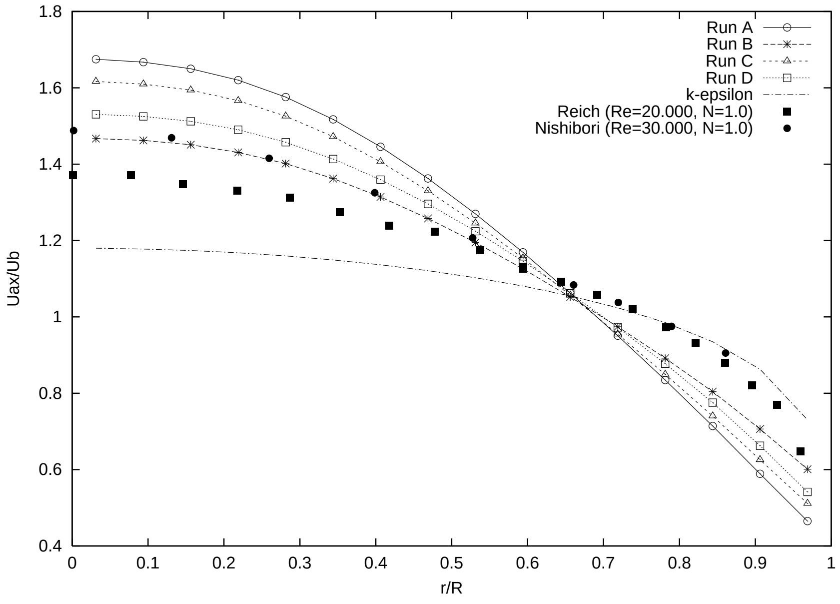

Figure 5.6: *Axial velocity profile normalized by U_b for the rotating pipe*

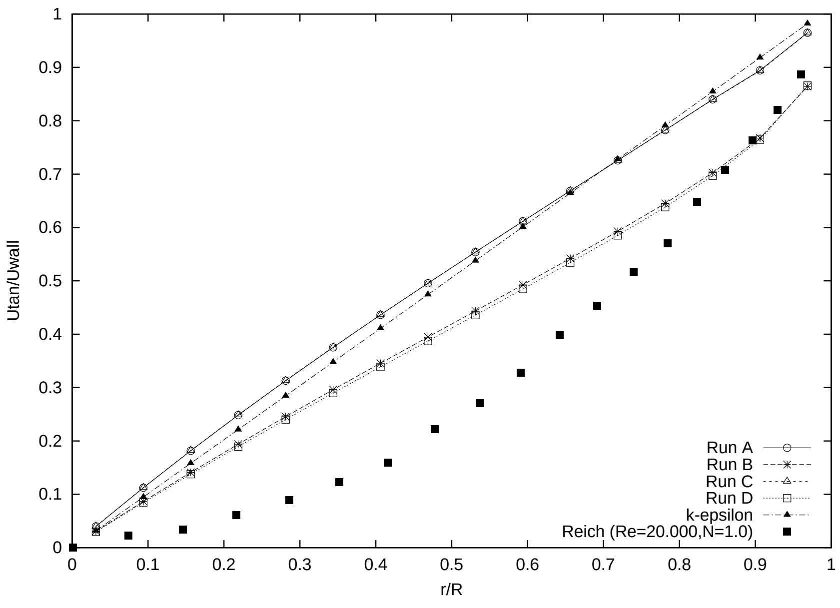

Figure 5.7: *Tangential velocity profile normalized by $u_{\theta,wall}$ for the rotating pipe*

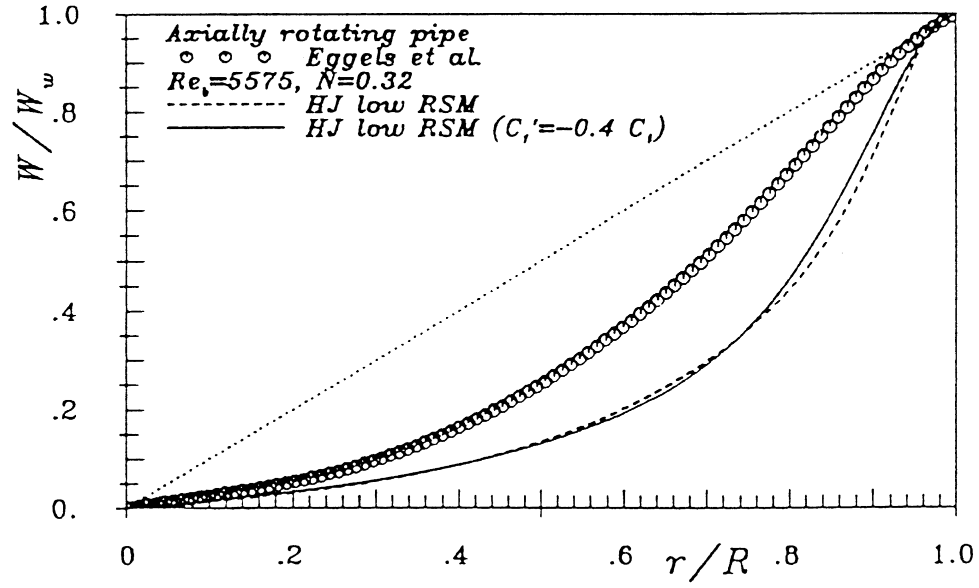

Figure 5.8: *Tangential velocity profile normalized by $u_{\theta,wall}$ for the rotating pipe (Jakirlic(1997))*

Chapter 6

Simulations of decaying swirling flows

6.1 Introduction

To investigate the performance of CFX when simulating decaying swirling flows we used the experimental data produced by Kitoh(1991) for comparison. He used a test pipe with a length of 7 meter and a internal diameter of 0.15 meter (fig. 6.1). Air was the working fluid. The Reynolds number based on the bulk velocity and pipe diameter was 50.000. Measurements were done at six positions along the axis, see tabel 6.1:

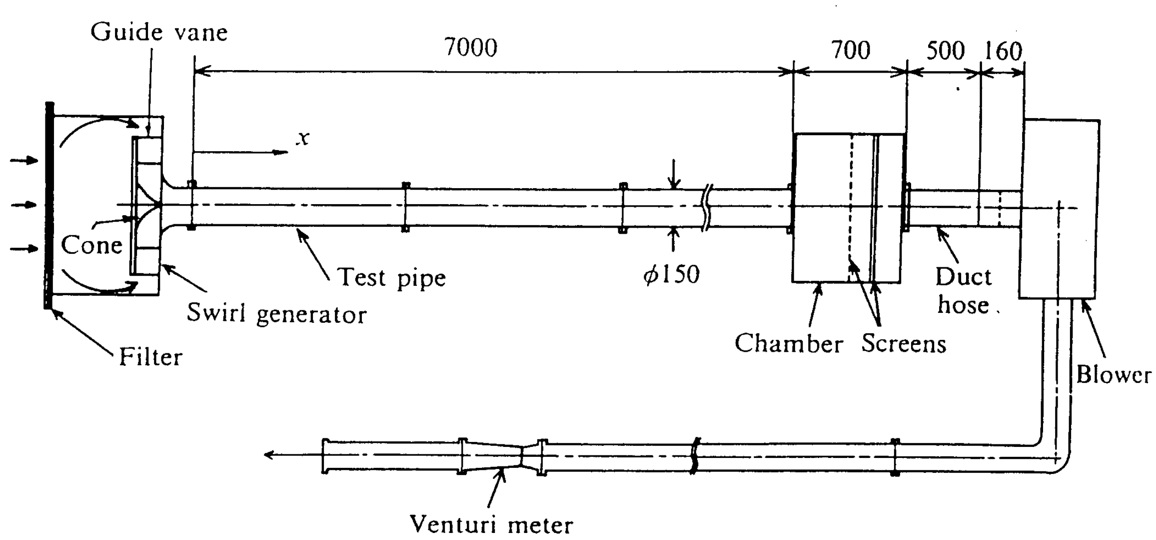

Figure 6.1: *Experimental setup*

Testsection	Position	x/D
TS1	850 mm	5.7
TS3	1850 mm	12.3
TS5	2850 mm	19.0
TS7	3850 mm	25.7
TS9	4850 mm	32.4
TS10	5850 mm	39.0

He measured the axial and tangential velocity profiles as well as the turbulent normal and shear stresses. To investigate the decay of the swirl in the pipe the swirl intensity (or swirl number) Ω was calculated at the different testsections. It is defined as:

$$\Omega = 2\pi\rho \frac{\int_0^{r_0} U_z U_\theta r^2 dr}{\rho \pi r_0^3 U_b^2}, \tag{6.1}$$

and can be interpreted as the dimensionless angular momentum flux. At the inlet the swirl intensity is about 1 and we will expect to see an exponential decay along the pipe axis (see Kitoh(1991)). Chen(1992) did a performance study of various turbulence models using the PHOENICS computer code developed by CHAM developement team (1991) which is a comparable CFD program as CFX4.2 and we will use some of his data for comparison. He used the conventional logarithmic law near the wall but did not specify the value of the constant C_μ in his report. He also tried to improve the performance of the Reynolds Stress model by altering various turbulence constants. CFX does not show notable improvements when varying the constants in the same way.

6.2 Simulations without wall reflection terms

The first set of runs was done without the use of the wall reflection terms, default turbulence constants and with all flow quantities set zero except for the axial and tangential velocities. We used the axial and tangential velocity profiles at TS1 as inlet boundary conditions. The axial velocity profile has a reversed flow in the core region (see fig. 6.2). In this case the inlet condition imposes a in- and outflow region.

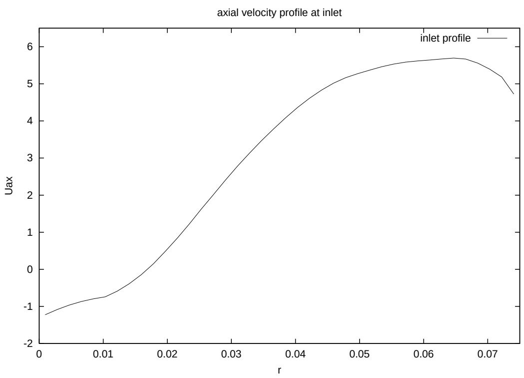

(a)

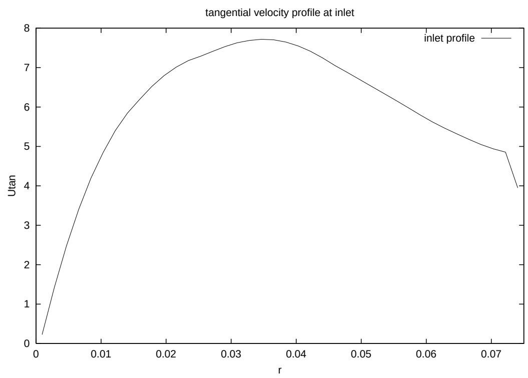

(b)

Figure 6.2: *Velocity profiles used for inlet conditions*

The radial velocity and the Reynolds stresses were set zero at the inlet. An axi-symmetric steady state simulation was done using the same gridspacing as Chen(1992), which was a $40 \times 40 \times 1$ axisymmetric simulation. To ensure a grid independent solution we also did a $80 \times 80 \times 1$ run and found no notable differences. Considerable problems with convergence were overcome using underrelaxation factors, Courant number false timesteps and the Algebraic Multigrid (AMG) solver. It was also necessary to start up with the $\kappa - \varepsilon$ model and gradually increase the tangential inlet velocity during the runs to ensure convergence. Several runs were done with different differencing schemes and no notable differences were found. Eventually we used a higher order upwind scheme for all simulations. We were able to get a steady state converged solution for this flow.

Turbulence constants	$Chen(DSMa)$	$CFX4.2(RSM)$
C_μ	unknown	0.09
C_1	1.8	1.8
C_2	0.6	0.6
C_s	0.22	0.22
C_1'	0.5	0.5
C_2'	0.3	0.3
C_ε	0.18	0.16
C_{ϵ_1}	1.45	1.44
C_{ϵ_2}	1.90	1.92

This gave the following result:

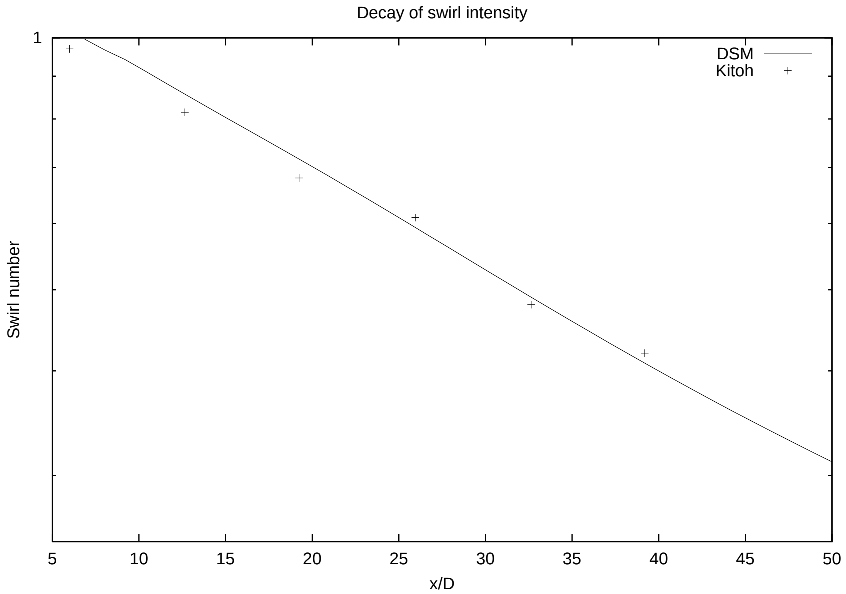

Figure 6.3: *Decay of swirl intensity*

The axial velocity profiles (see fig. 6.4) show good agreement with Kitoh(1991) except that we have less reverse flow at the centerline. The RSM runs perform better than than ASM and DSMa runs done by Chen(1992). There is a reasonable agreement when we look at the tangential velocity profiles in fig. 6.5. In fig. 6.5(f) one can see the peak of the tangential velocity moving towards the centreline of the pipe as the flow developes downstream. This is conform the experiments. The swirl intensity decays in a similar way as Kitoh(1991). We found an exponential decay (see fig. 6.3) and this is in contrast to the findings of Chen(1992). However the ASM data produced by Chen(1992) does show a exponential decay of swirl but underpredicts it. In figures 6.6 - 6.10 the Reynolds shear and normal stresses are shown. At the first two sections TS3 and TS5, the stresses are considerable lower than the DSMa run by Chen(1992) and in better agreement with Kitoh(1991). This can be explained by the fact that in this run our Reynolds Stresses at the inlet were set zero and needed to develope downstream while Chen(1992) prescribed inlet profiles obtained from the experimental data at TS1. Remarkable is the agreement of RSM with data obtained from runs using the Algebraic Stress Model. The reason for this could be that the ASM run was done with the same inlet conditions as our RSM run. Also some ASM stress profiles show strange peaks which could indicate a not fully converged solution. We had considerable convergence problems with CFX4.2 using the ASM model and eventually abandoned the model and focused on the RSM model. At test sections TS3, TS9 and TS10 we have a reasonable agreement for the shear stresses but a overprediction for the normal stresses.

6.3 Simulations with wall reflection terms

We also did an additional run including the wall reflection terms and with the modified $C_\mu = 0.065$ (Run D). It was necessary to run a transient simulation on the last run to obtain a converged solution. The stabilizing effect of running transient simulations is explained in appendix A. The timestep Δt was set at 0.005 seconds. We used the same inlet conditions as in the previous run which means that we only prescribed the axial and tangential velocity profiles and set all the Reynolds stresses and dissipation rate zero. The results are shown in figures 6.11, 6.12 and 6.13 where we compared them with the run from the previous section without wall reflection terms and $C_\mu = 0.09$ (run A) and with the experimental results.

The axial profiles are allmost identical for the runs A and D. The tangential velocity profiles however are slightly higher for Run D then for Run A. This is caused by the decrease of the wall shear stress as discussed in the previous chapter. This effect can also be seen in figure 6.11 where we have a slower decay of the swirl intensity. We did not include the Reynolds stress profiles as they are more or less the same and the effect of the wall reflection terms on these profiles has been discussed in the previous section.

We also tried to simulate the flow prescribing the Reynolds stresses and dissipation rate at the inlet. We used the turbulent stress profiles at TS1 from Kitoh(1991) and used the following relation for the inlet dissipation rate:

$$\epsilon = \frac{\kappa^{\frac{3}{2}}}{0.2 \times D}, \tag{6.2}$$

which is the same relation Chen(1992) used. κ represents the turbulent kinetic energy and D is the pipe diameter. We used the resolved velocity field from the previous run to start our simulation. It was not possible to get a converged solution with a steady state or transient simulation.

6.4 Conclusions

We can conclude that the Reynolds stress model gives reasonable mean-flow quantities results but underpredicts the reverse flow region. When including the wall reflection terms and modifying C_μ the decay of swirl is slower compared to Run A. In this case Run A seems to give the best results allthough the difference between Run A and Run D is small.
Furthermore it is extremely difficult to obtain a convergent solution with a swirling flow using the Reynolds stress model. It was for instance not possible to get a converged solution when we prescribed the six Reynolds stresses and the dissipation rate at the inlet. However the data produced CFX is better compared the Chen(1992) when we look at the decay of swirl intensity.

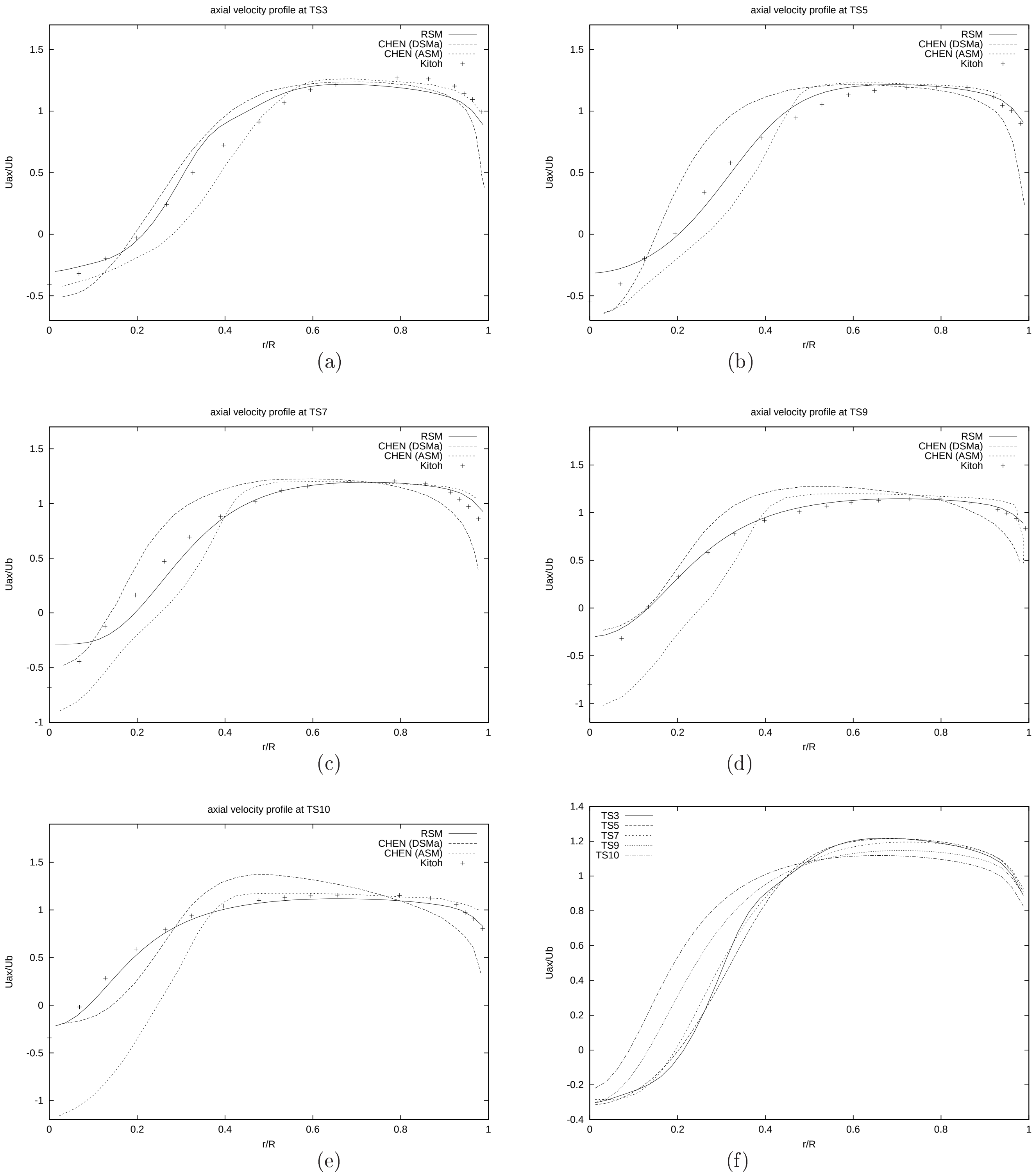

Figure 6.4: *Normalized axial velocity profiles at different axial positions along the pipe axis*

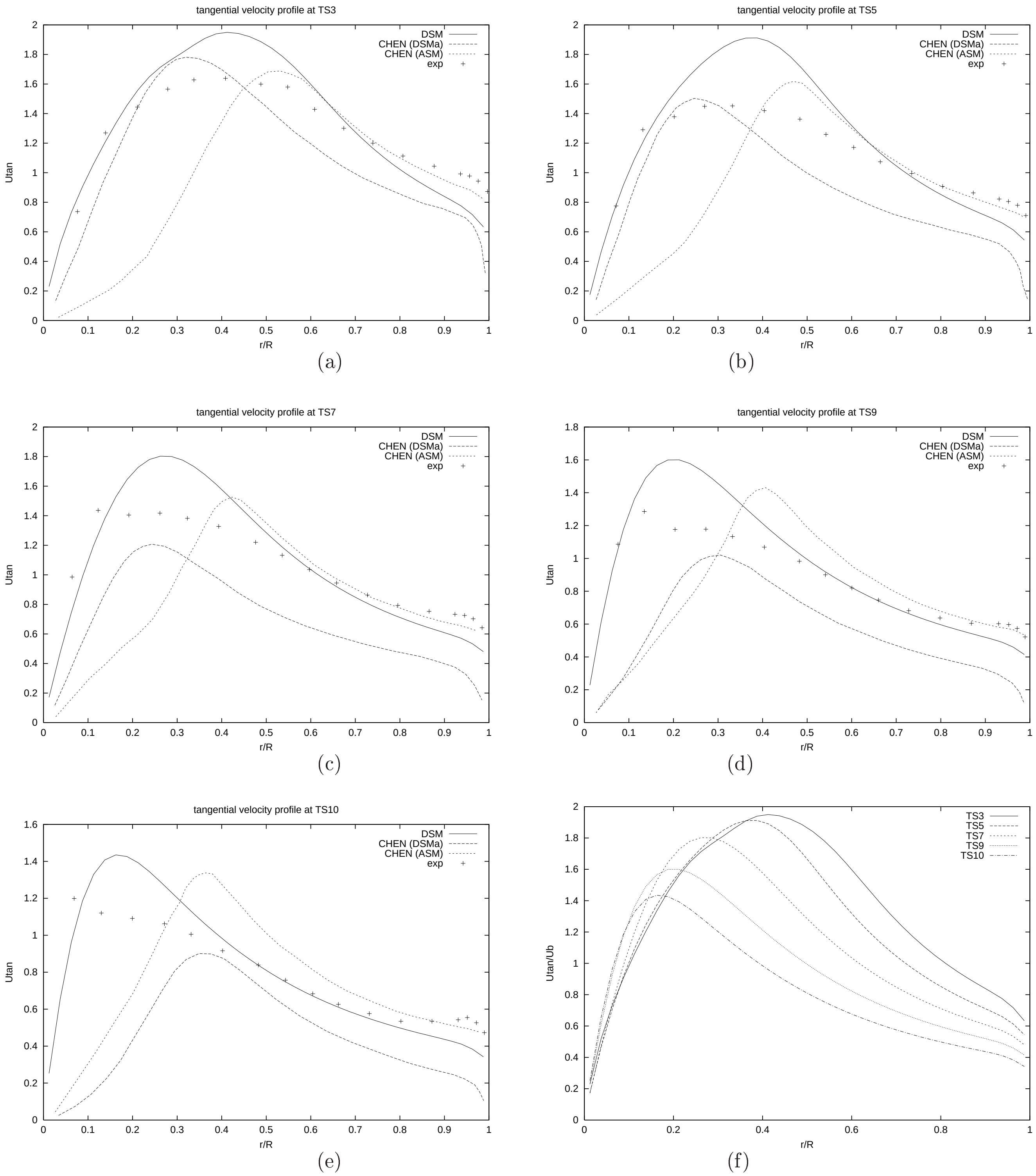

Figure 6.5: *Normalized tangential velocity profiles at different axial positions along the pipe axis*

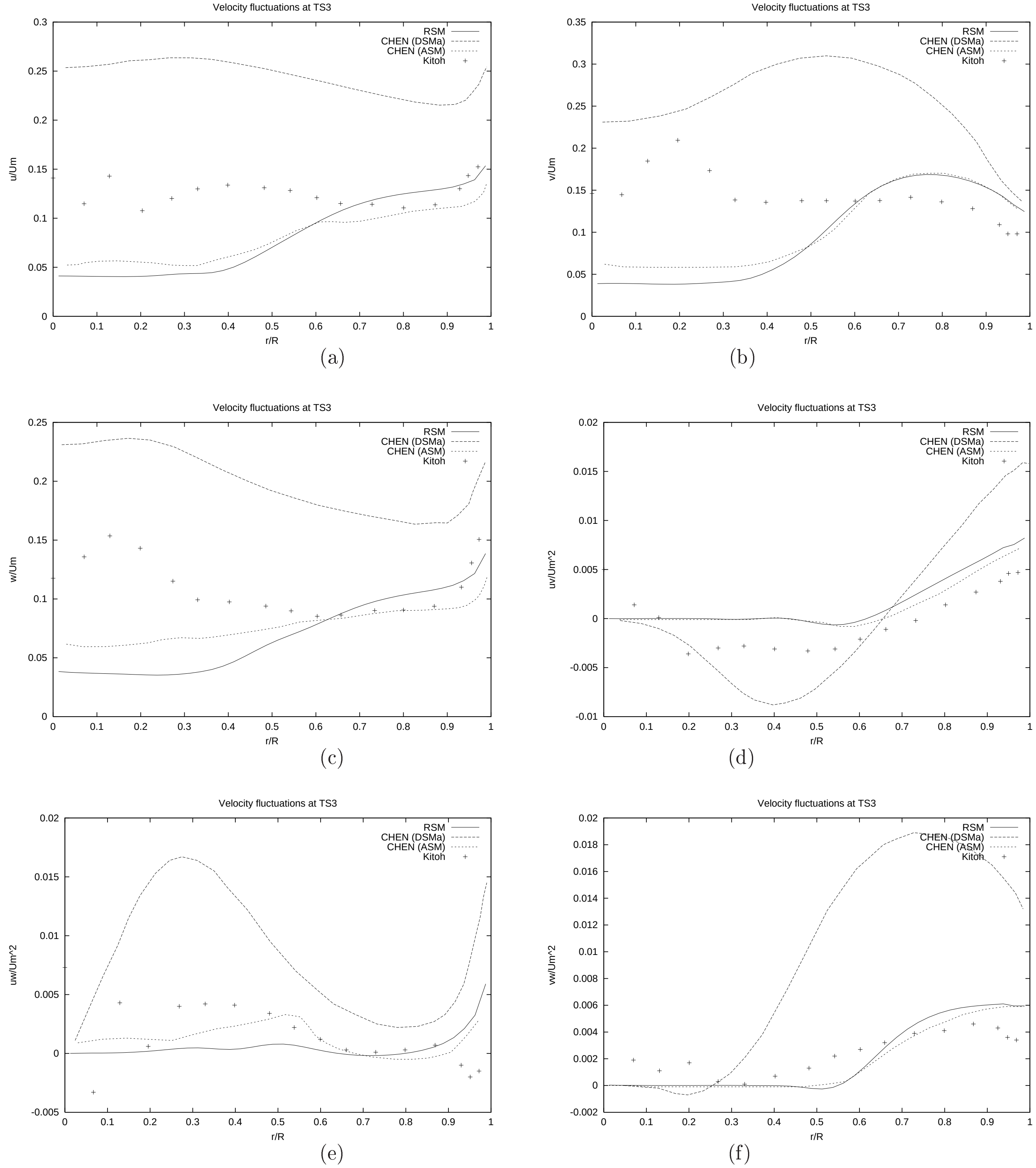

Figure 6.6: *Normalized Reynolds normal and shear stresses at TS3*

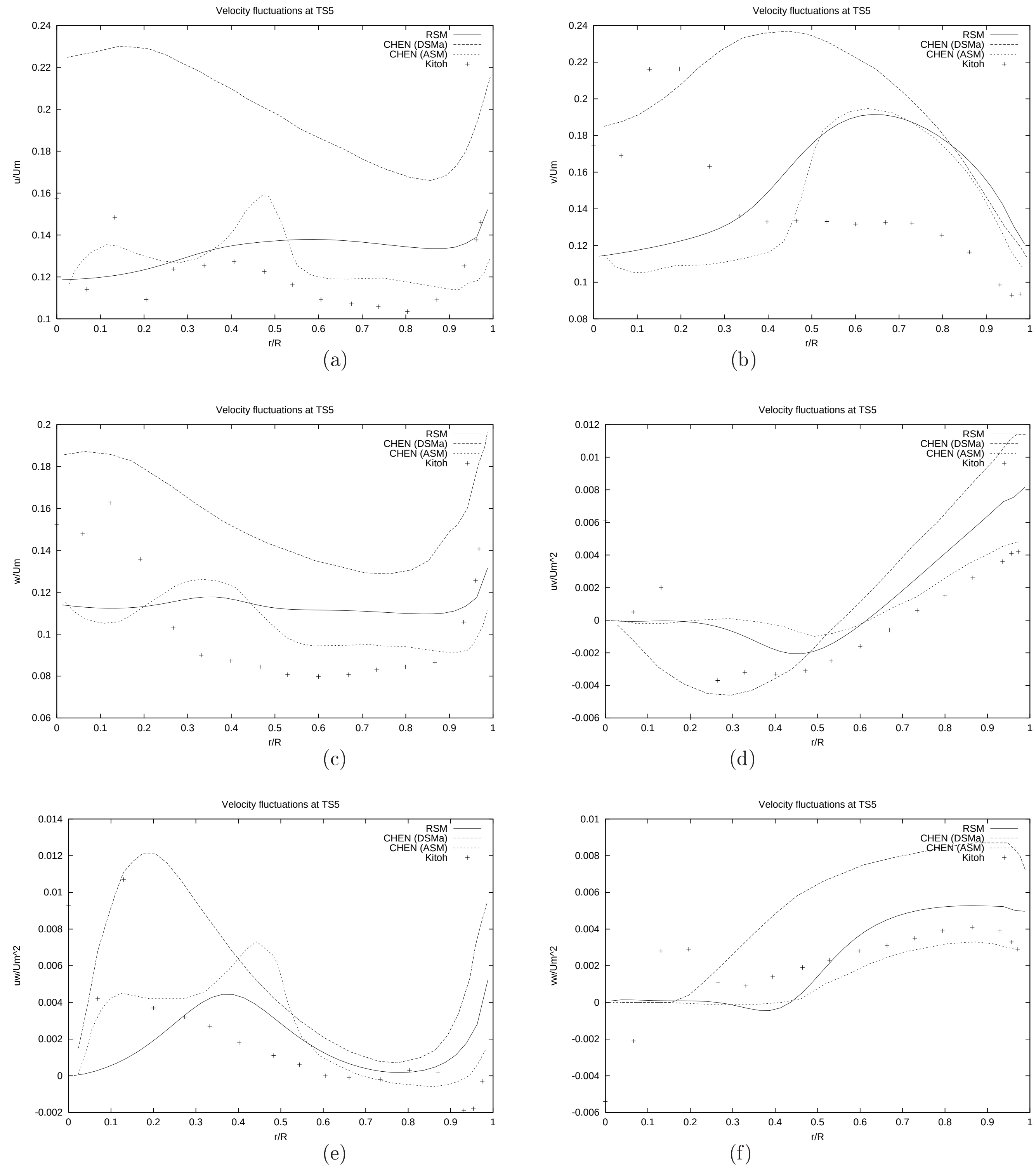

Figure 6.7: *Normalized Reynolds normal and shear stresses at TS5*

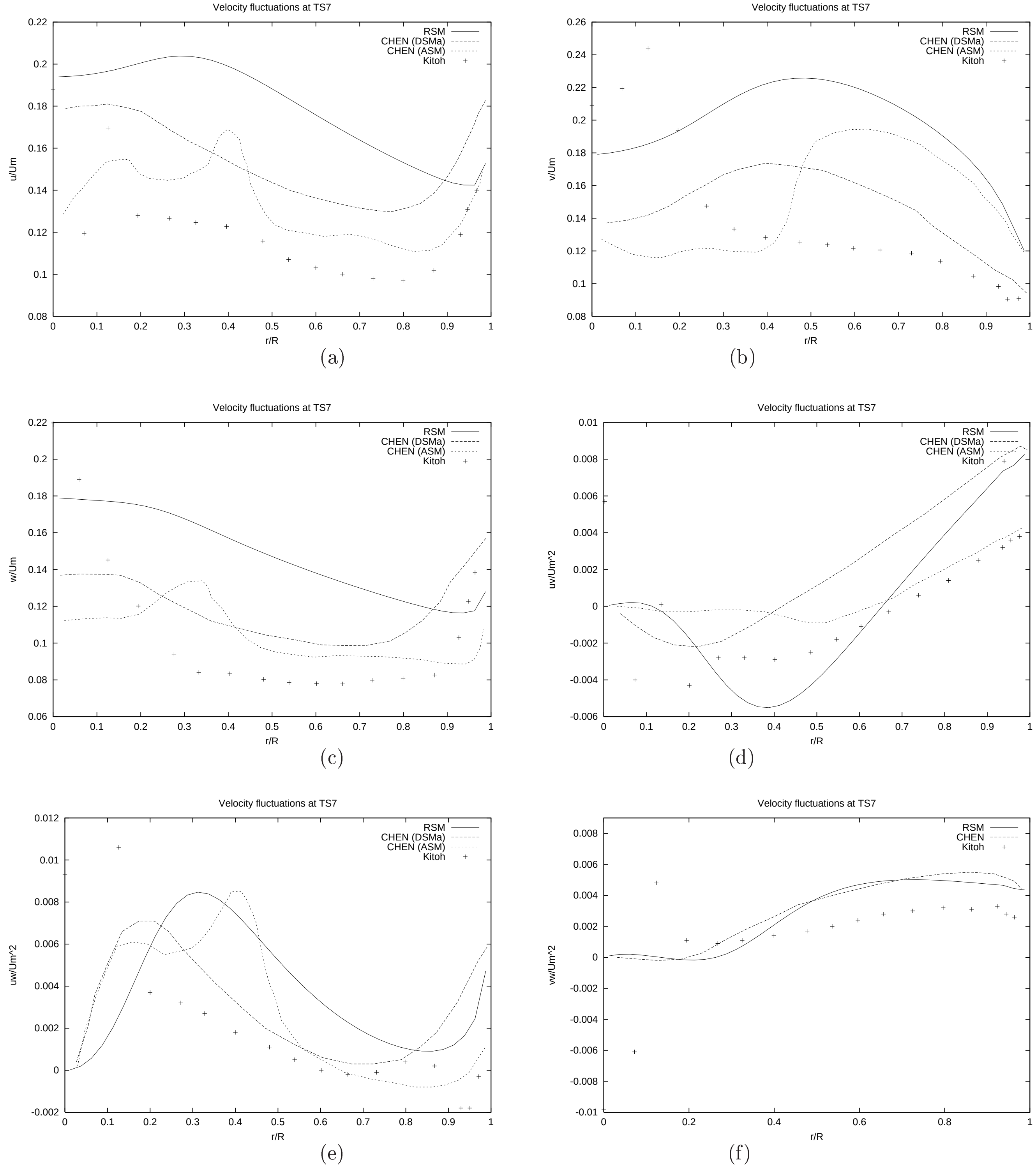

Figure 6.8: *Normalized Reynolds normal and shear stresses at TS7*

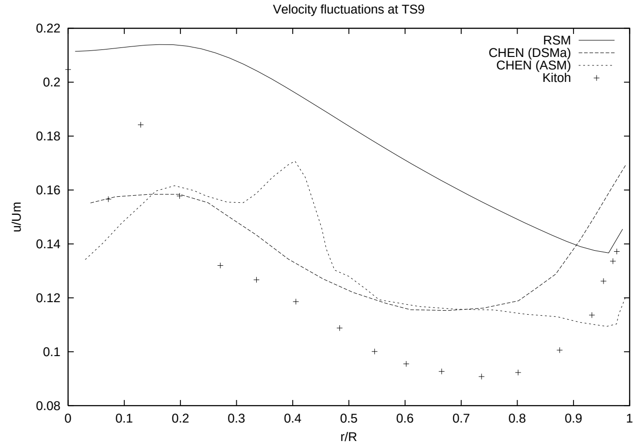

(a)

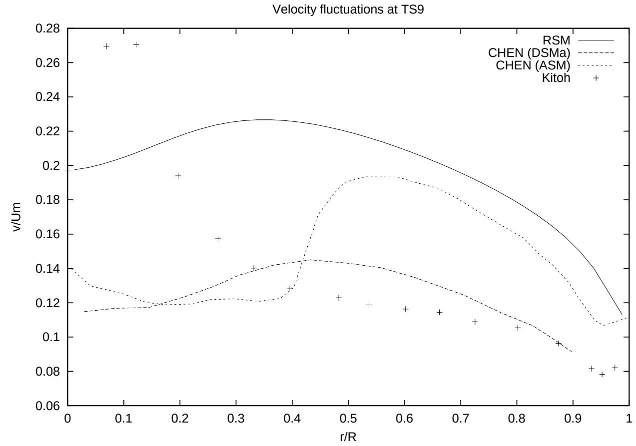

(b)

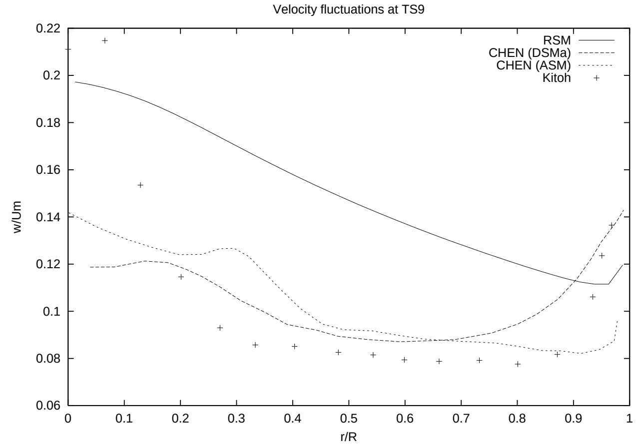

(c)

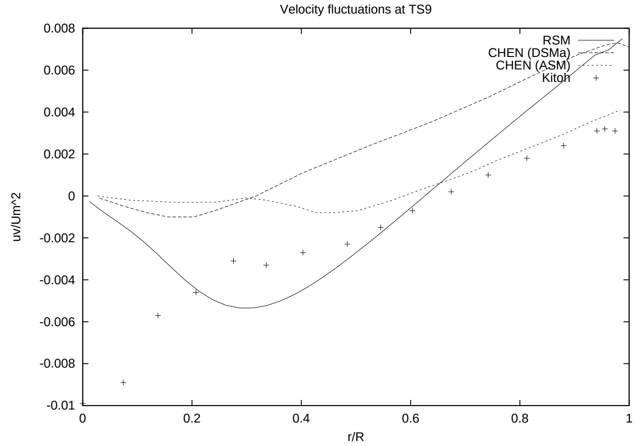

(d)

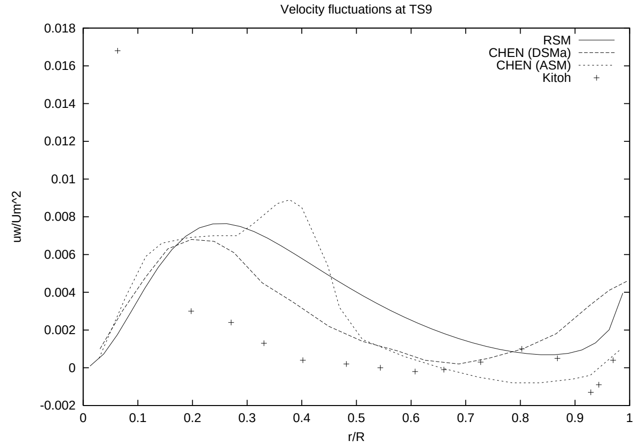

(e)

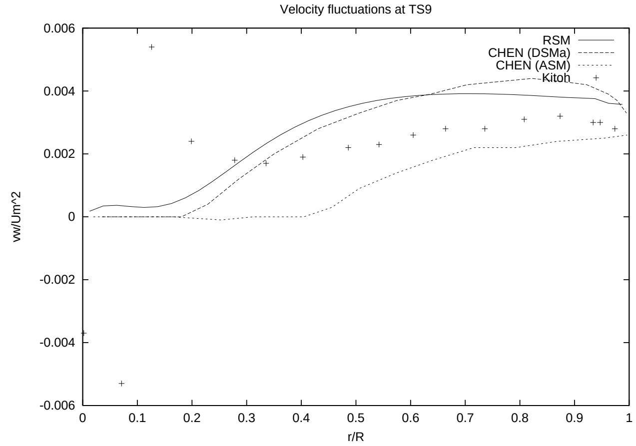

(f)

Figure 6.9: *Normalized Reynolds normal and shear stresses at TS9*

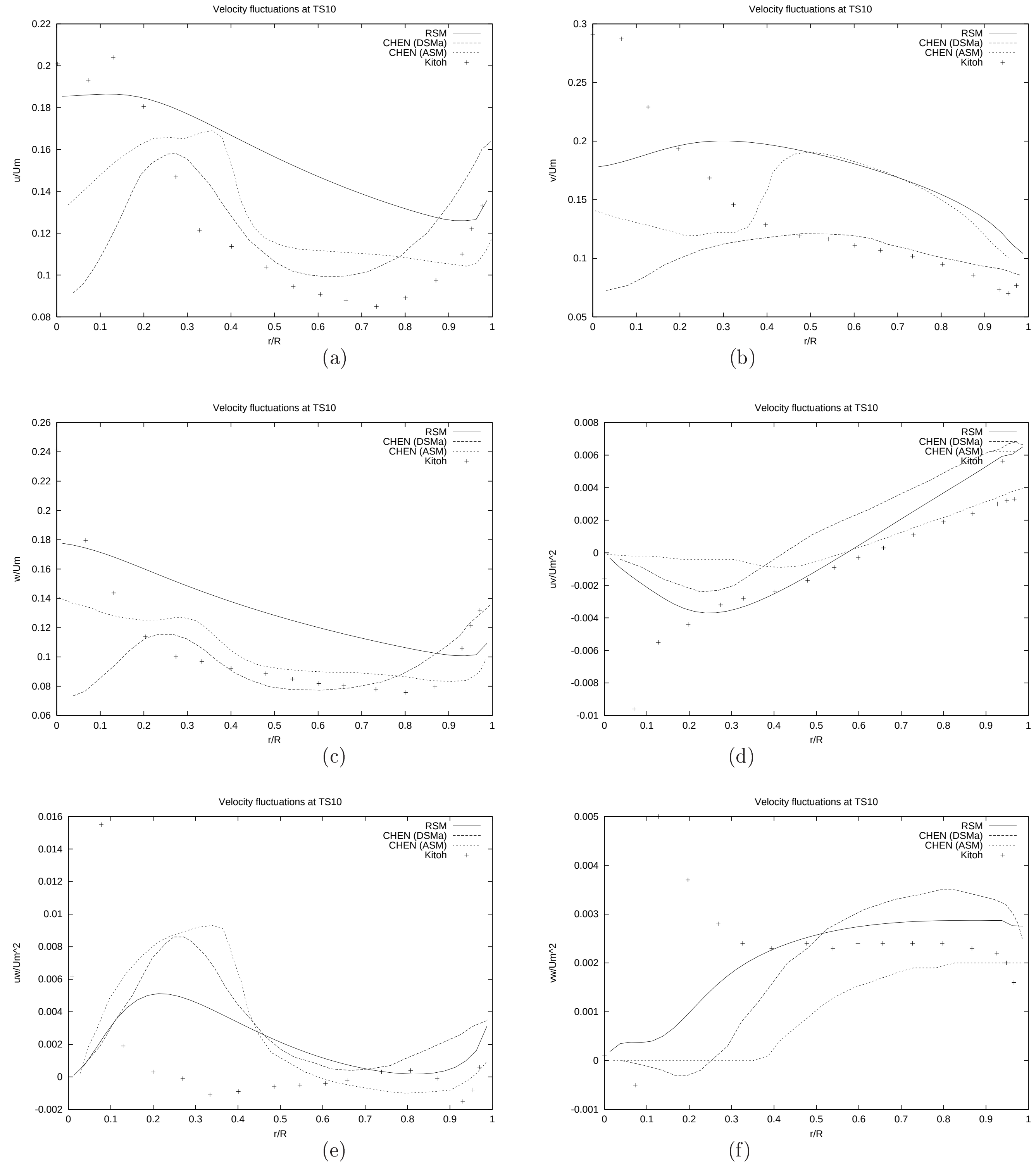

Figure 6.10: *Normalized Reynolds normal and shear stresses at TS10*

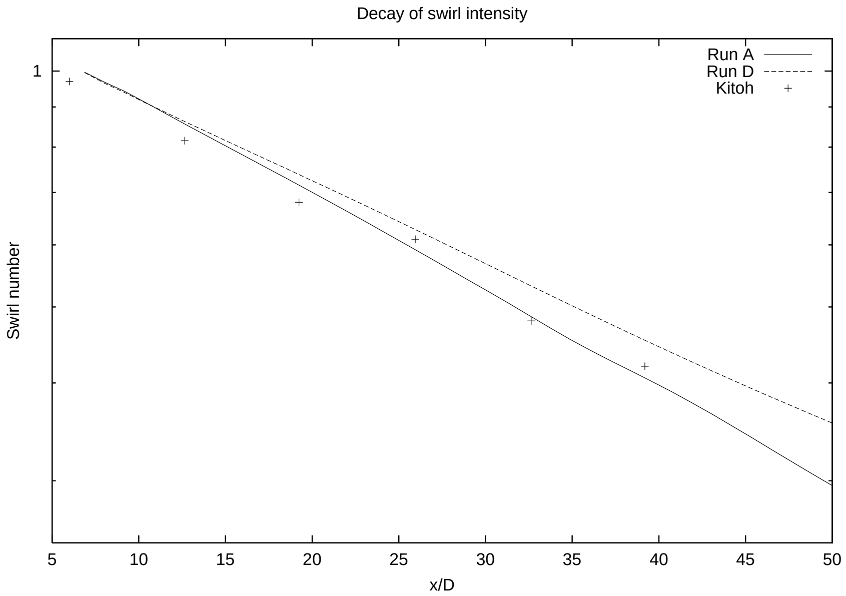

Figure 6.11: *Decay of swirl intensity*

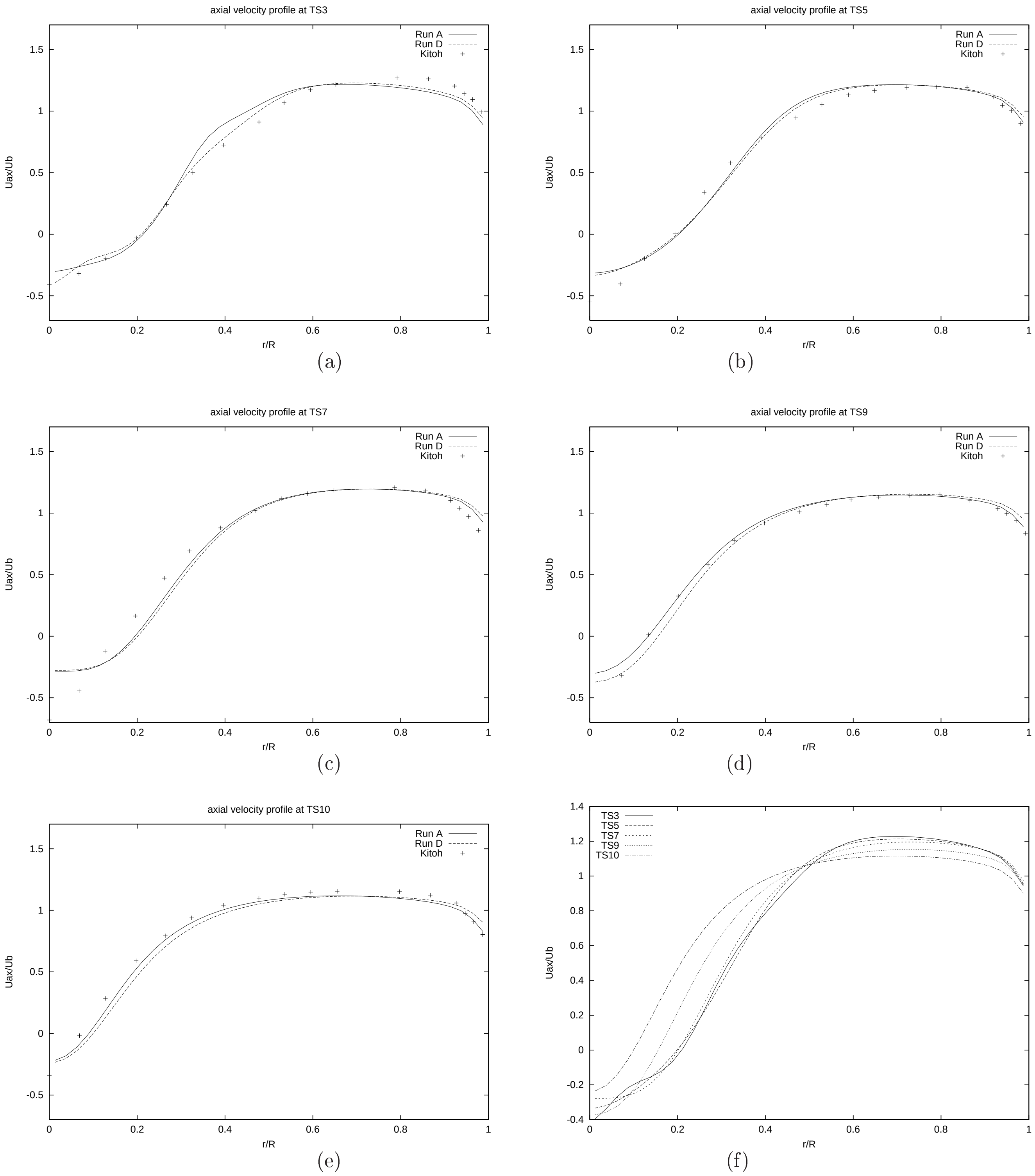

Figure 6.12: *Normalized axial velocity profiles at different axial positions along the pipe axis*

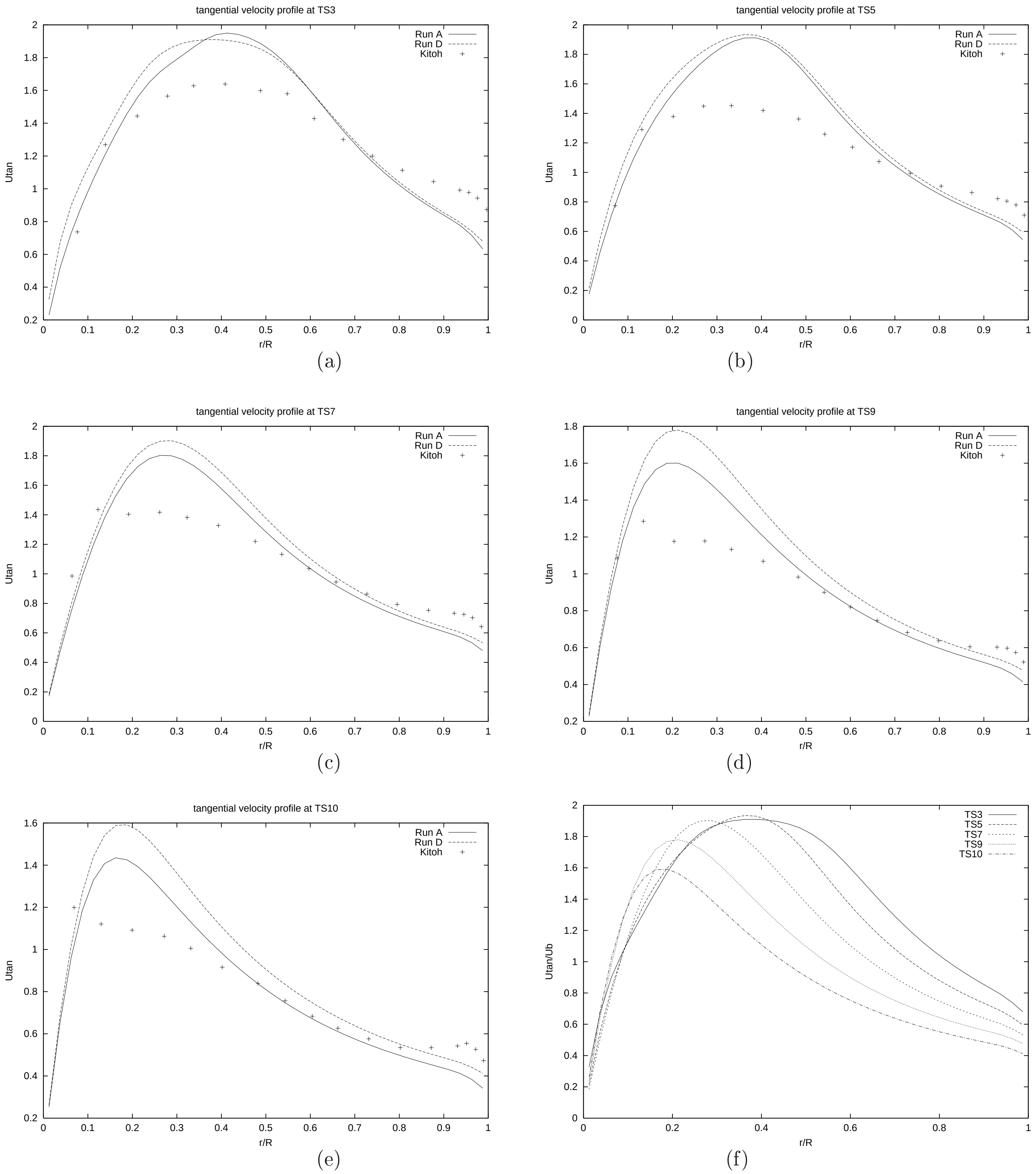

Figure 6.13: *Normalized tangential velocity profiles at different axial positions along the pipe axis*

Chapter 7

Cyclone flow calculations

7.1 Introduction

Dirkzwager(1996) did measurements on a cylone which consisted of a swirl generator and a straight pipe. He did several measurement series with different initial values by varying the swirl intensity and axial velocity. Measurements were done at six different positions downstream in the straight pipe. No measurements were done in the inlet section. We did axi-symmetric runs with $Re_b \approx 4.8 \times 10^4$ and the 72n design for the swirl generator, see fig. 2.1. We encountered considerable convergence problems. Eventually we obtained convergence by running transient simulations with a time step $\Delta t = 0.005s$. The possible reasons for this can be that we are dealing with a non-stationary flow or that the numerical problems are caused by a badly conditioned matrix (This is explained in Appendix A), or a combination of both.

The other reason for the convergence problems could be that we are dealing with a instationary flow. Swirling flows sometimes show an oscillatory motion of the vortex centre which is called Precessing Vortex Core (PVC) (see Dirkzwager(1996)) .This is a 3-dimensional motion so we can't investigate this phenomenon as we are doing axisymmetric simulations ($\partial/\partial\theta$=0).

In the inlet section (fig. 7.10) we can see a so called Ekman-boundary layer. At the lower wall of the inlet section there is a strong increase of axial velocity and a large negative radial velocity between x=0.2 m. and x=0.6 m. After this layer we see a area with a strong increase of the radial velocity. This could indicate a separation point and we investigated this point for instationarity by using a monitoring point at $(x, r) = (0.2725, 0.0116)$ during Run A. We did not observe any oscillation of the three velocity components so we can conclude that the seperation point is stationary. We also placed a monitoring point at $(x, r) = (3.074, 0.001)$ during Run A. This point is near to the pipe axis at the end of the reverse flow region so we can invesigate if this region is moving back and forth along the pipe axis. The results are shown in figure 7.1. Figure (fig. 7.1(b)) is to illustrate the difference between a stationary point and our monitoring point.

The results are not very spectacular (Note the different scaling of the vertical axis!). The axial velocity in figure a is oscillating but the difference between minimum and maximum is only 0.04% of the mean velocity. It is not very likely that our convergence problems are caused by this (minor) instationarity. It is more likely that the problems are of a numerical nature.

7.2 Results

We did several simulations on different different grid spacings and obtained a grid-independent solution with the grid spacing as shown in tabel 7.2 and figure 7.2.

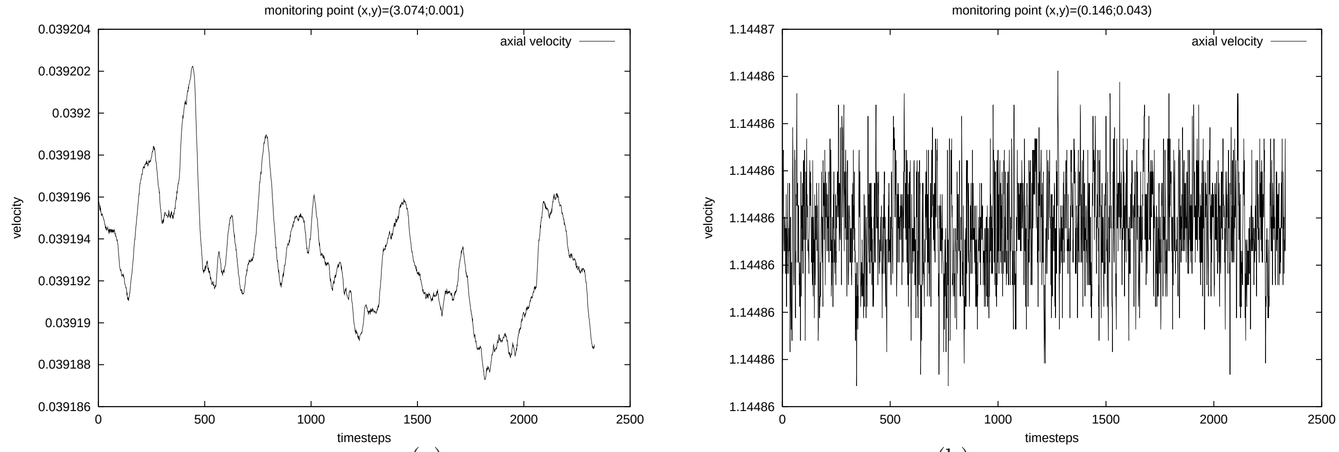

(a) (b)

Figure 7.1: *Axial velocity oscillations at different monitoring points*

Section	Mesh seed type	Number of elements	L_2/L_1 ratio
Inlet Section radial	Two way bias	20	20
Inlet Section axial	One way bias	48	48
Pipe Section radial	Two way bias	20	20
Pipe Section axial	One way bias	110	110

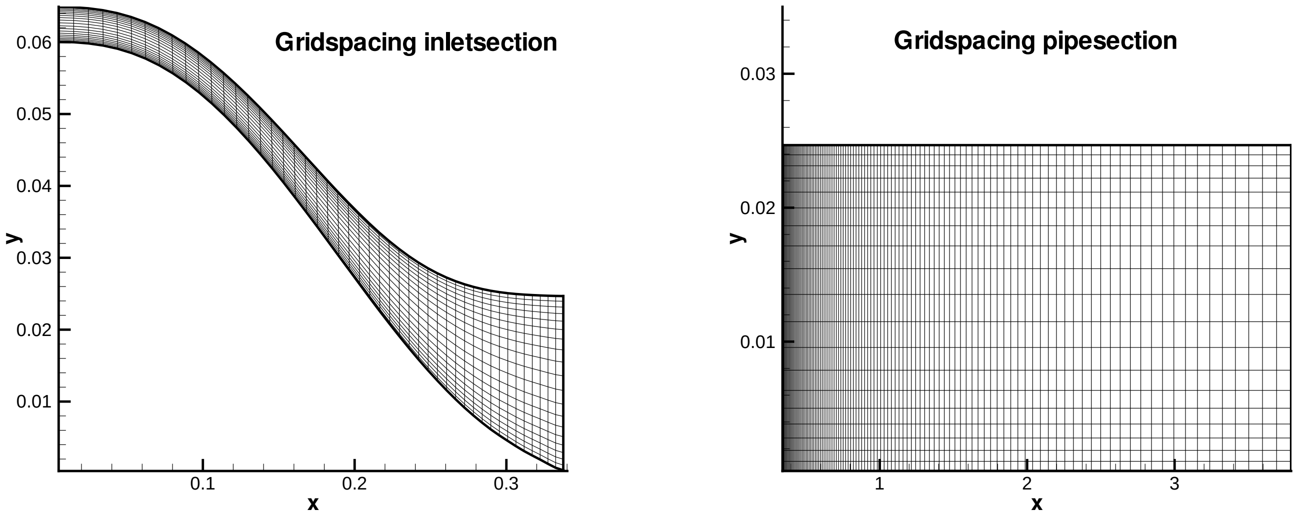

(a) (b)

Figure 7.2: *gridspacing*

We did four sets of runs, see tabel 7.2. With runs C and D we varied C_μ which was suggested by CFX (This is previously discussed in chapter 5). We expect a stronger decay of the swirl when we increase C_μ. However this is not the case as we can see in figure 7.8

Run	Wall reflection terms	C_μ
A	no	0.09
B	yes	0.09
C	no	0.1152
D	yes	0.065

We used the default values for all the other turbulence constants. The results are shown in figures 7.3-7.8 and discussed in section 7.3.
For illustration see figure.

7.3 Discussion

Axial velocity profiles

All the different runs are incapable of producing the correct axial velocity profiles for the first 5 testsections. There is allmost no reverse flow region in the first four testsections. At the last section (x/D=60) Run B shows the best similarity when we look at the maximal reverse flow but overpredicts the width of the reversed flow region. This behaviour is also shown in figure 7.11 where we see the streamline patterns of the different runs. You can clearly see that there is a second recirculation cell in every run. This has also been observed by Leibovich & Faler (1977) and Garg & Leibovich (1979). Dirkzwager(1996) did not find a similar second recirculation cell in his experiments.

Tangential velocity profiles

It is now no suprise that the tangential velocity profiles will not match Dirkzwager's as we are dealing with a different axial velocity field. Nevertheless we will discuss them to get some insight in the working of the wall relection terms and the influence of C_μ.
We can see that the peak of the profiles move towards the centreline which is the same behaviour as the experimental. The influence of the wall reflecion terms is demonstrated nicely in the different plots (figure 7.4 when you compare Run A with Run B. Run A gives an underprediction and Run B an overprediction. This is what can be expected due to the direct influence on $\overline{u'_z u'_r}$ as discussed in chapter 5. Without the wall refelction terms we have an overprediction of the radial velocity fluctuations $\overline{u'_r u'_r}$ which is the dominant term in the production P_{zr} (eq. 5.11) of shear stress ($\overline{u'_z u'_r}$). By adjusting C_μ the results do get 'better'. At the last test section (x/D=60) we again see that the profiles match quite well.

Axial velocity fluctuations $(\overline{u'_z u'_z})^{\frac{1}{2}}$

At the wall we see clearly the influence of the wall reflection terms for run B and D where rms-values are higher than for run A and C. This is what we expected as the radial velocity fluctuations are damped near the wall and transfer energy to the streamwise velocity fluctuations. The influence of the wall reflection terms reaches over the entire radial domain. The peaks in the experimental profiles are caused by the precessing vortex core. This is an asymmetric motion so it is no suprise that we do not find similar peaks in our runs. The profiles show reasonable agreement for the middle test sections but none of the runs is capable of producing good results for all the sections.

Radial velocity fluctuations $(\overline{u'_r u'_r})^{\frac{1}{2}}$

The peaks in the experimental profiles are again caused by the precessing vortex core so we need not to worry about them. We can see the damping of the radial velocity fluctuations near the wall for Run B and D and again the influence of the wall reflection terms reach over the entire radial domain. The last two test sections show reasonable agreement.

Reynolds stress $\overline{u'_z u'_r}$

Also for the shear stresses the profiles tend to match better as the flow develops more downstream. The first two test sections show nearly no shear stress in the centre of the pipe. We can see that the stresses are lower near the wall when we use the wall reflection terms.

7.4 Conclusions

The Reynolds Stress Model generates an extra recirculation cell for this geometry which was not observed by Dirkzwager. There can be several reasons for this:

-By doing an axisymmetric simulation we are not modelling the asymmetric features of the flow.

-Instead of modelling the swirl element we are imposing a uniform axial and tangential velocity profile at the inlet.

-We are using a wall function instead of resolving the flow near the wall. Unfortunately we have no choice as CFX implements a wall function automatically for all but the Low-Reynolds $\kappa-\epsilon$ models.

–According to Dirkzwager(1996) the wall region is not constant in the swirling pipe flow. The slope of the log profile decreases with increasing swirl number Ω. The decrease stops at $\Omega > 0.3$ where we have a constant value of the von Karman constant of $\kappa = 0.725$. To take this behaviour into account the von Karman constant should be a function of the swirl number. This is not possible in CFX.

-The wall reflection terms are only implemented for one wall so they are not used for the wall of the swirl element.

-The wall reflection terms are fit for straight walls (as in channel flows) and straight pipe walls. They are however not suitable for bent pipes. This means that the reflection terms are not calculated correctly in the inlet section

-CFX never updated the turbulence constants because they did not want users to find different results for identical problems run on different versions of their software. This means that the default constants are not necesarily the correct ones.

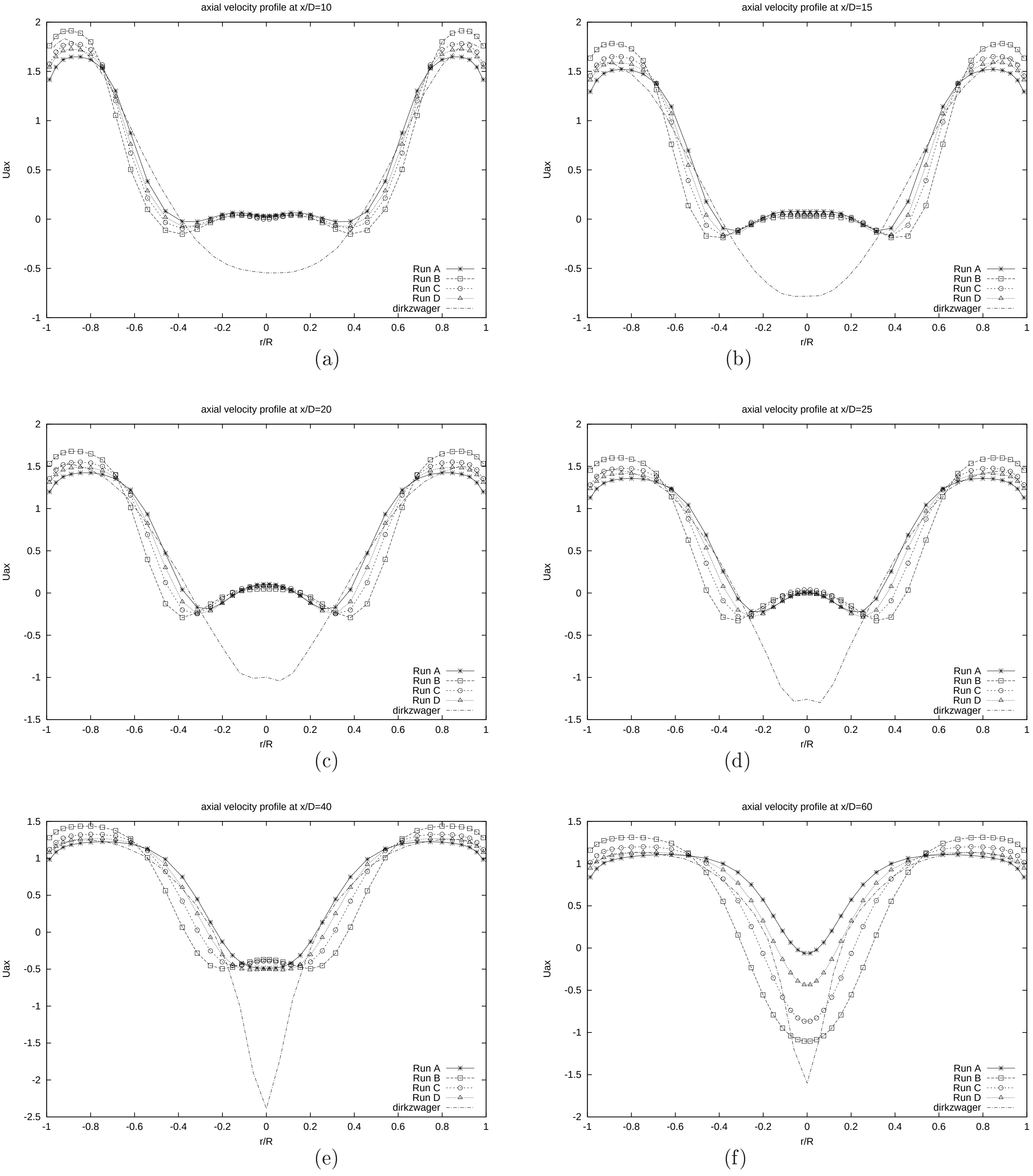

Figure 7.3: *Axial velocity profiles at different positions downstream*

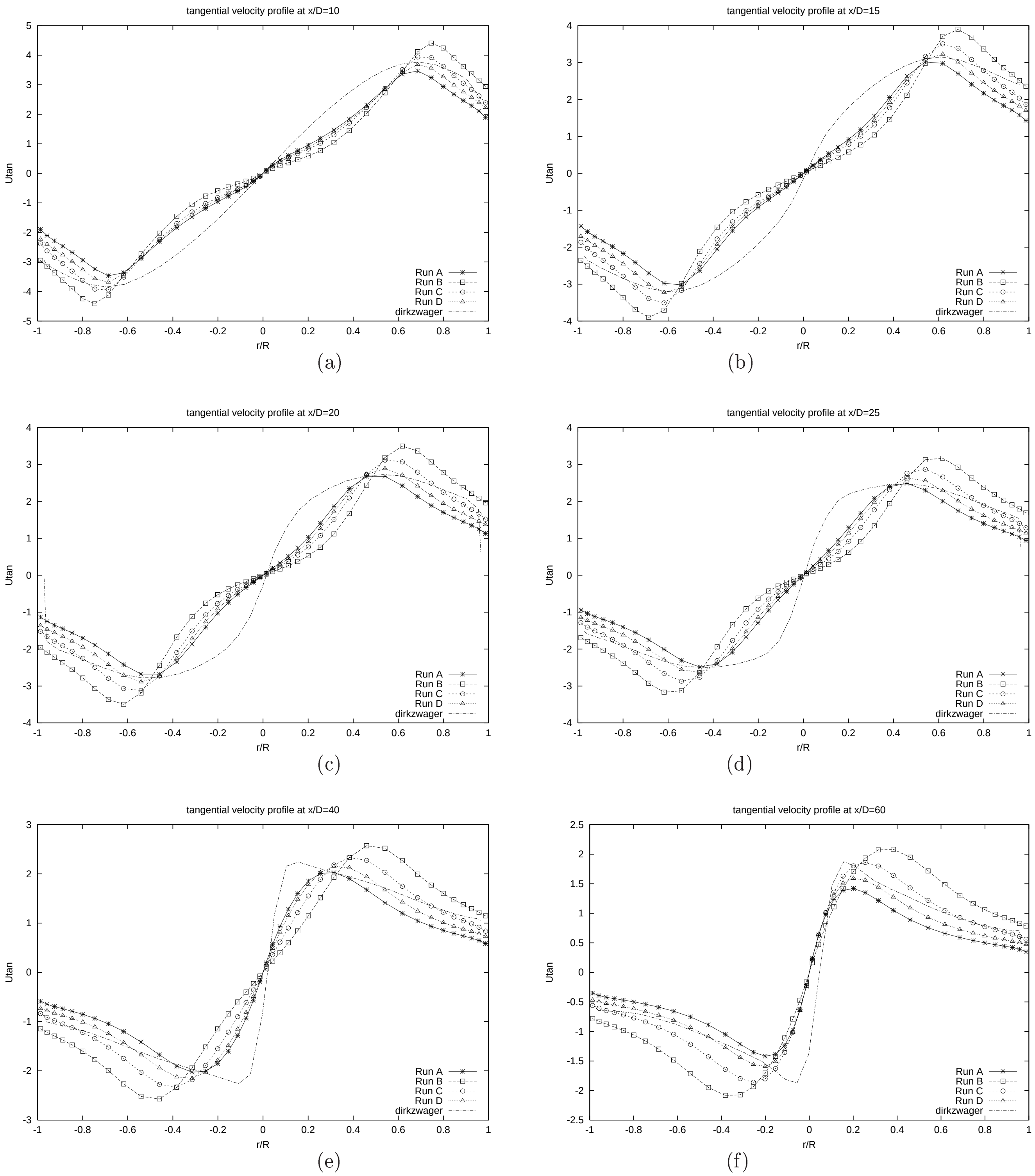

Figure 7.4: *Tangential velocity profiles at different positions downstream*

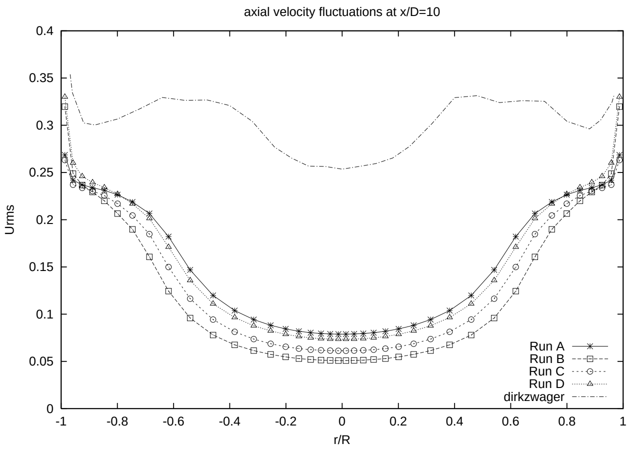

(a)

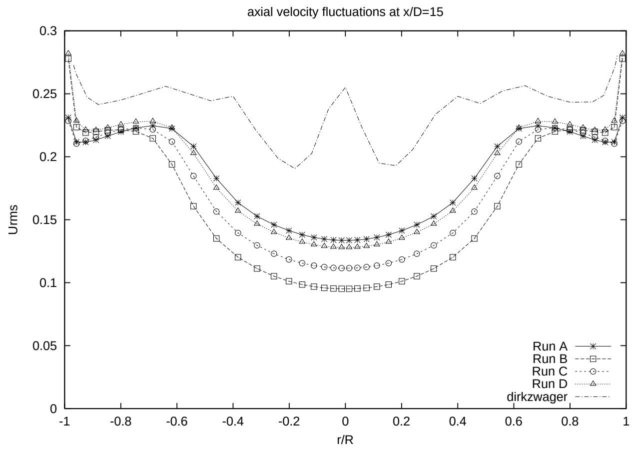

(b)

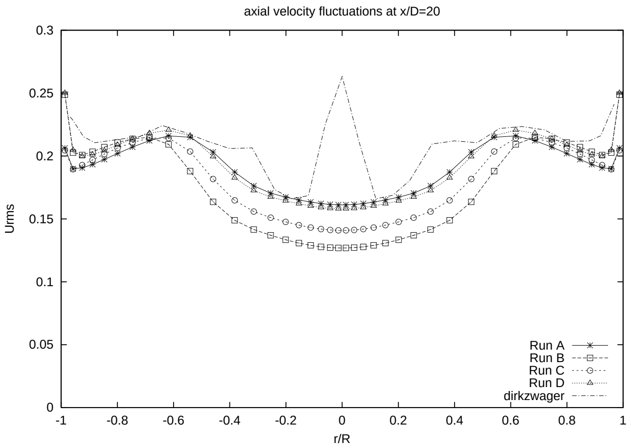

(c)

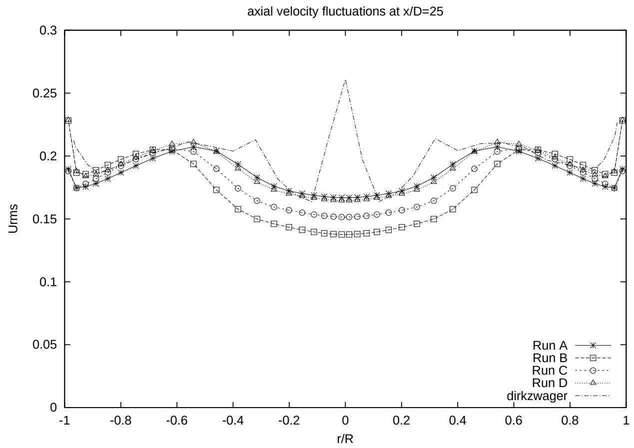

(d)

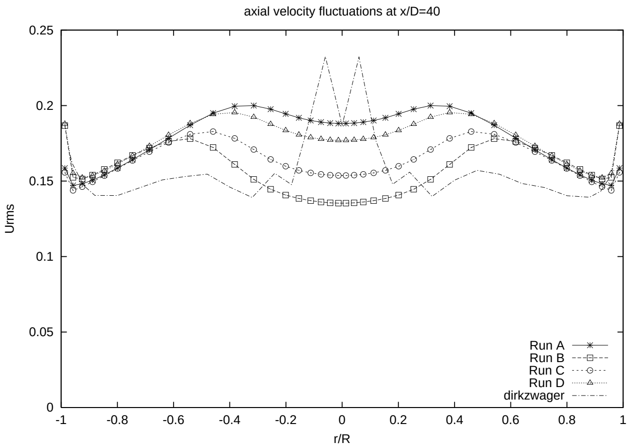

(e)

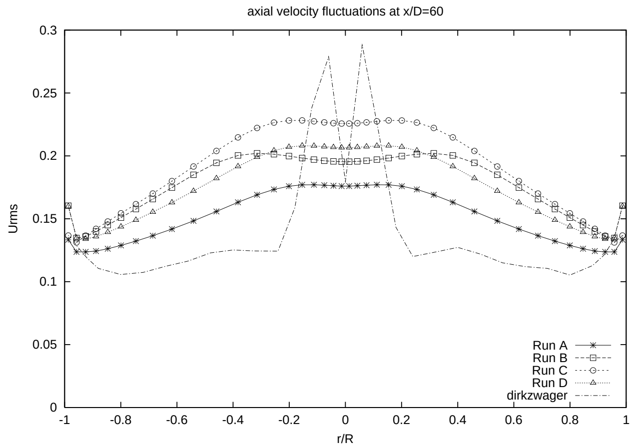

(f)

Figure 7.5: *The root mean square of the axial velocity fuctuations at different positions downstream*

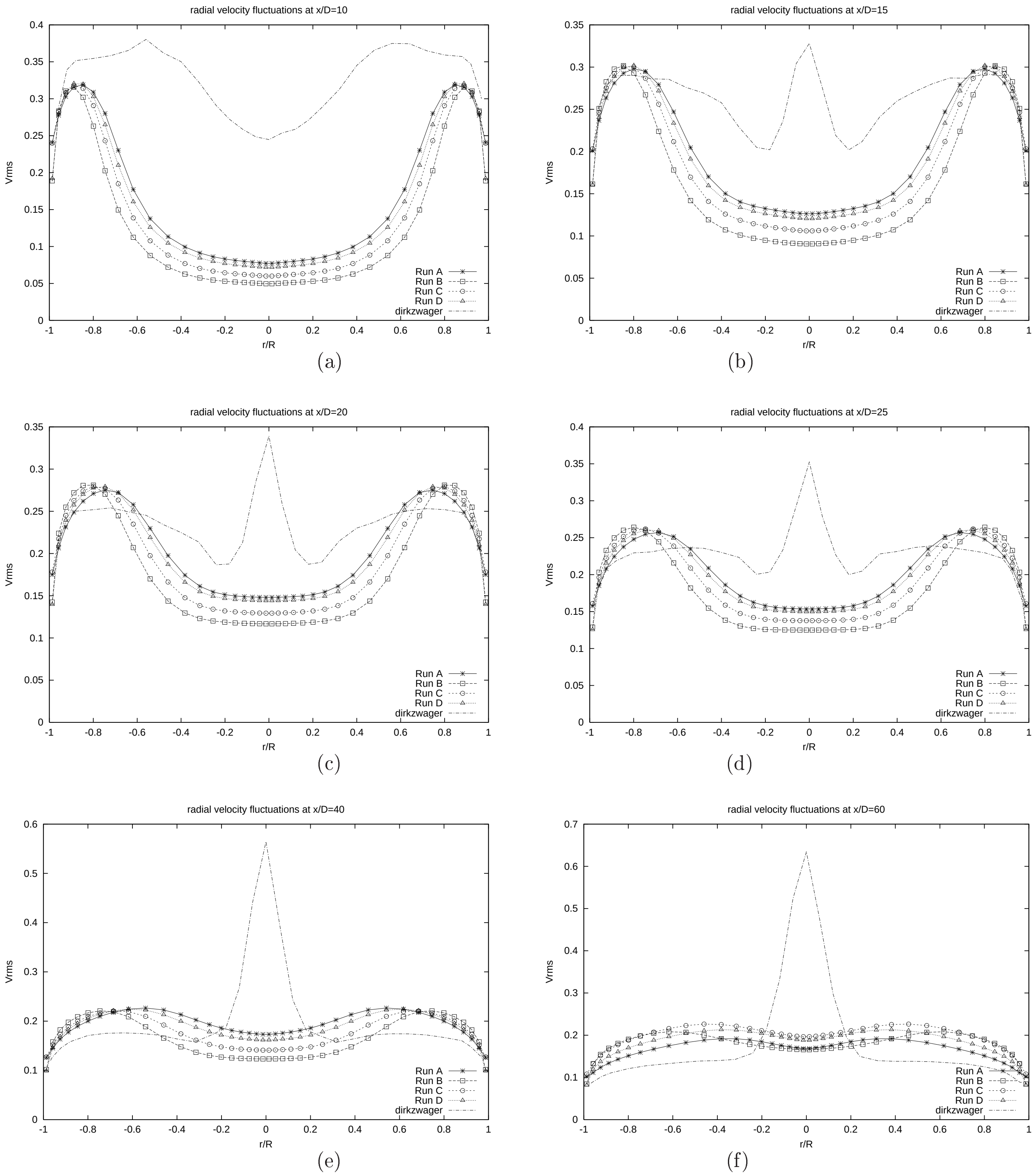

Figure 7.6: *The root mean square of the radial velocity fuctuations at different positions downstream*

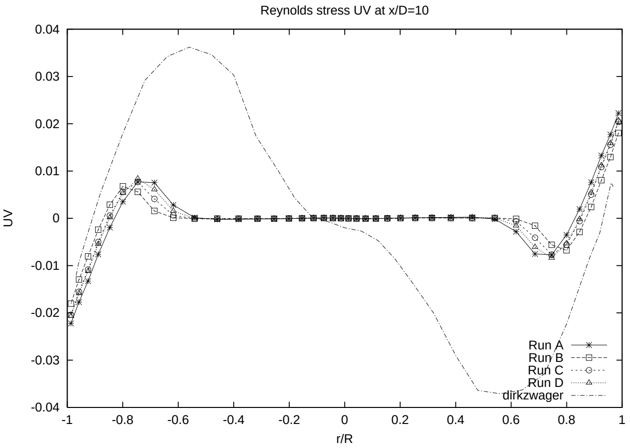

(a)

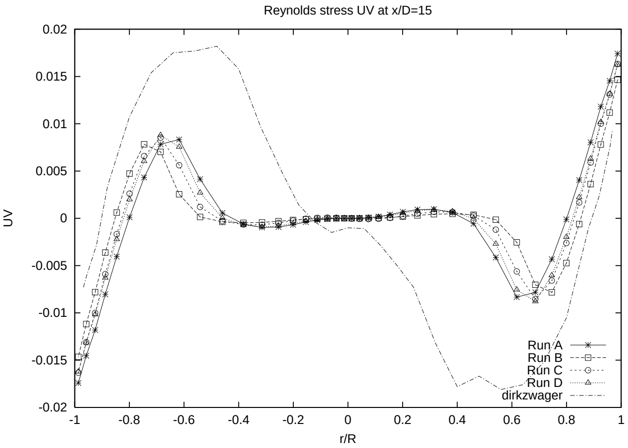

(b)

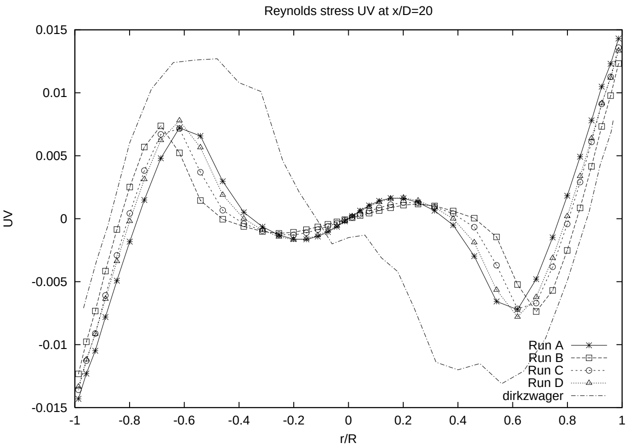

(c)

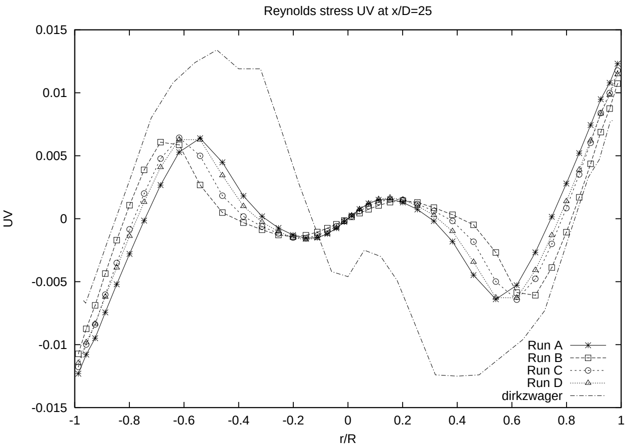

(d)

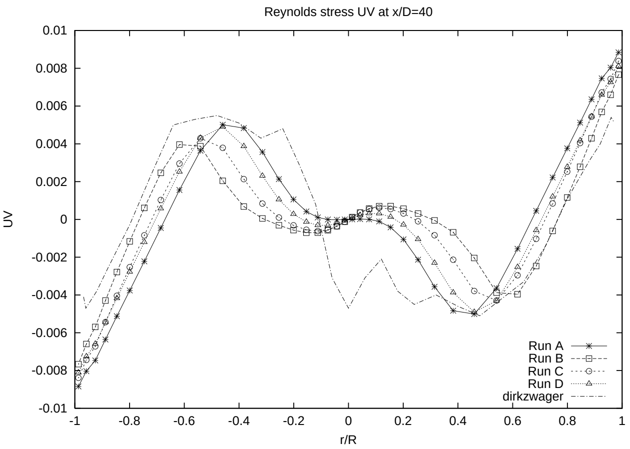

(e)

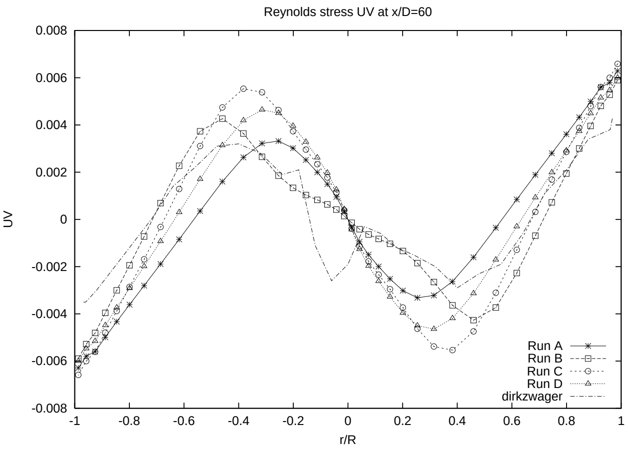

(f)

Figure 7.7: *The reynolds stresses* $\overline{u_z' u_r'}$ *at different positions downstream*

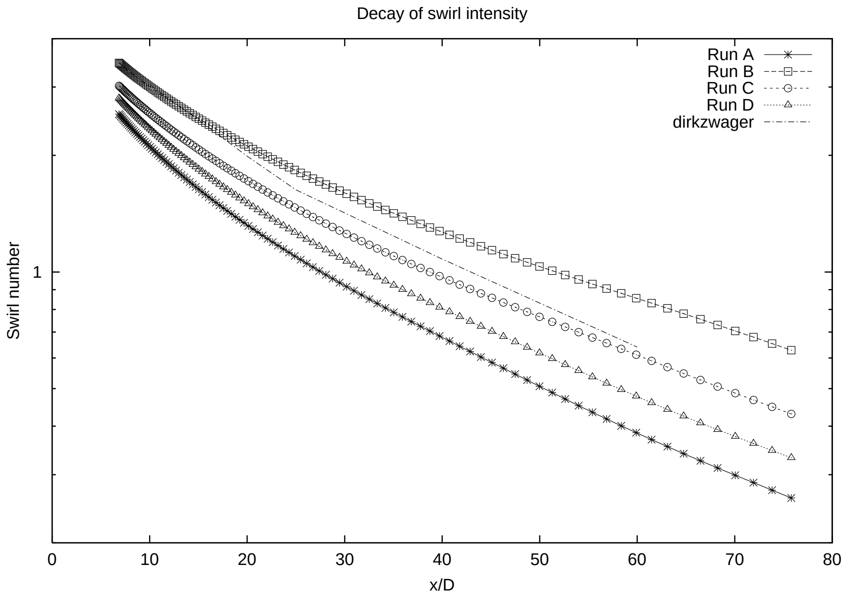

Figure 7.8: *Decay of swirl intensity*

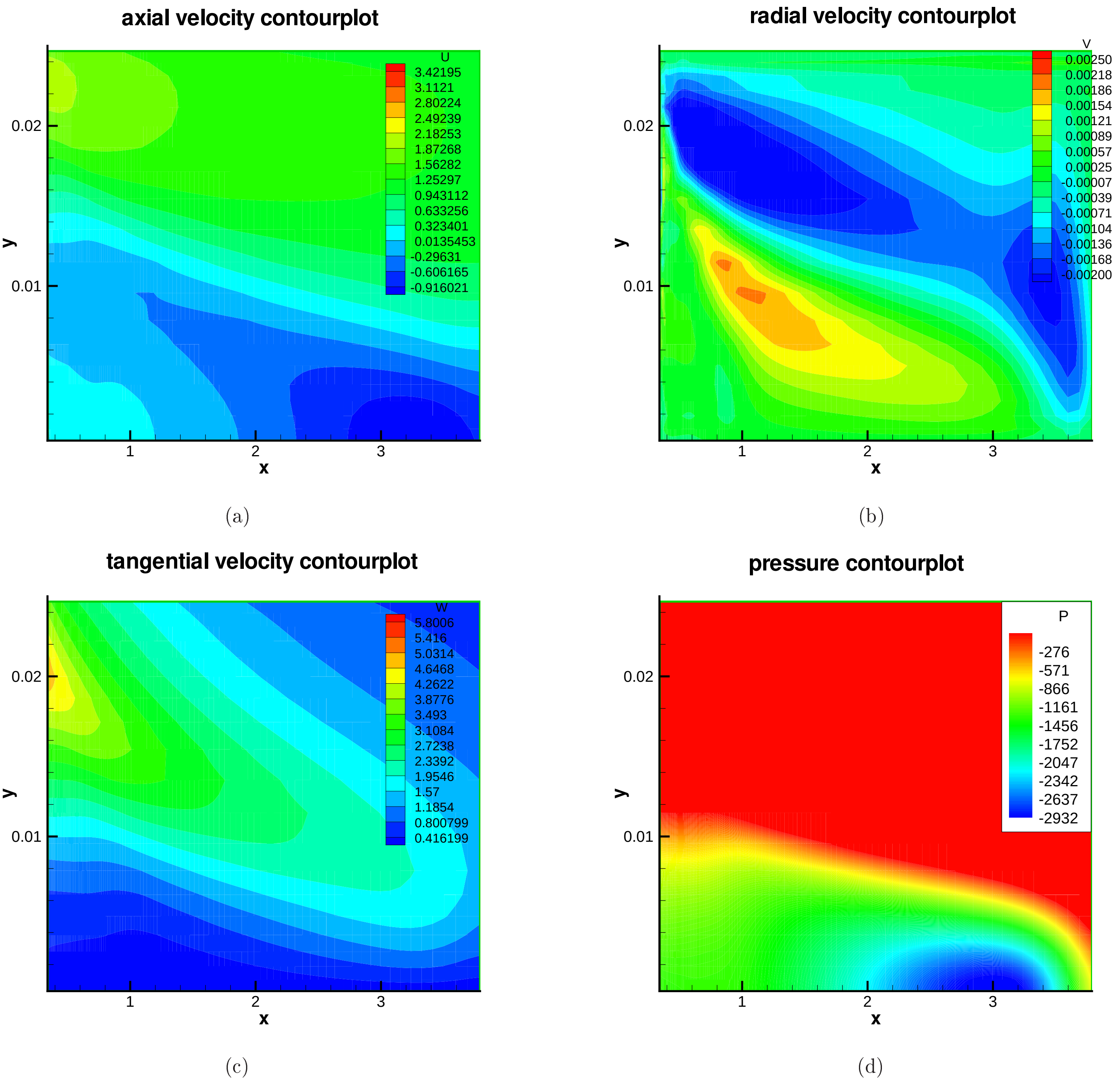

Figure 7.9: *Velocity and pressure contourplots at the outlet section. The color red in the pressure contourplot (fig. d) represents* $Pressure > 0\ Pa$.

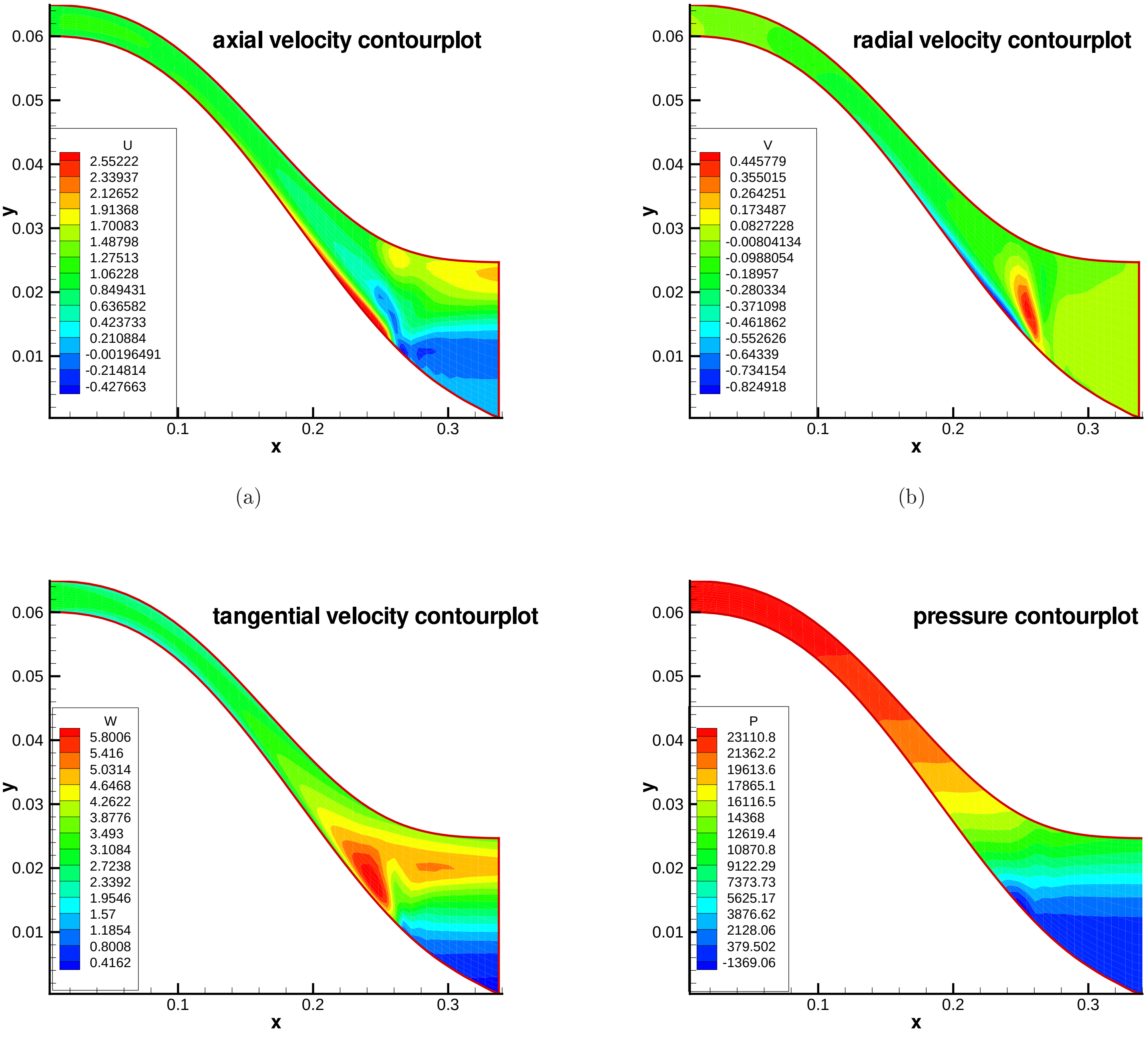

(c) (d)

Figure 7.10: *Velocity and pressure contourplots at the inlet section*

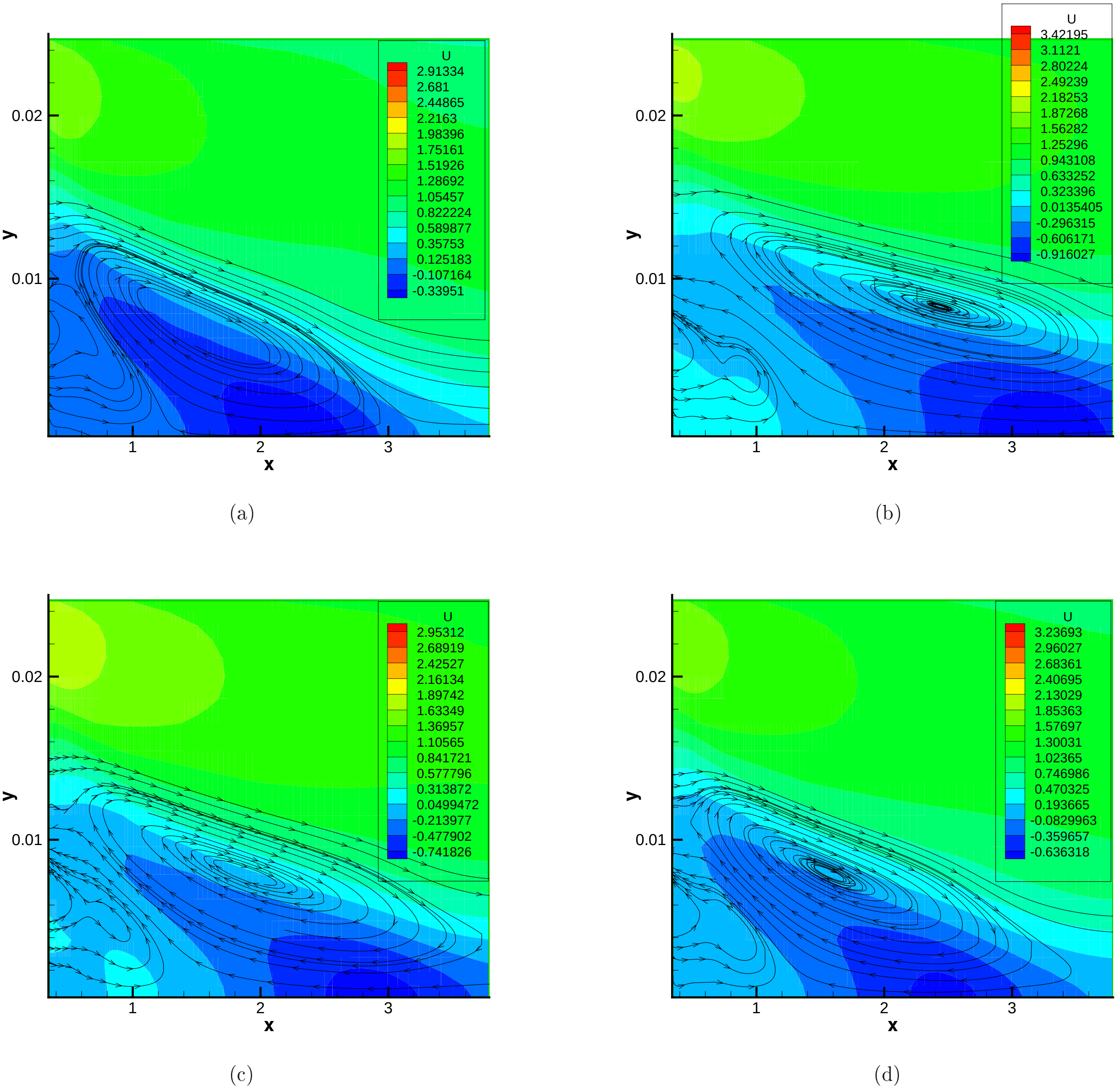

Figure 7.11: *Streamline patterns (a) Run A, (b) Run B, (c) Run C and (d) Run D*

Chapter 8

Conclusions and Recommendations

The conclusions of this study are the following:

1) The standard and RNG $\kappa - \epsilon$ models perform reasonably well for the non-rotating pipe flow but are not suitable for the rotating pipe flow. These models produce isotropic turbulence and for swirling flows they predict solid body rotation whilst experiments show different tangential (parabolic) and fluctuating (non-isotopic) velocity profiles.

2) The Algebraic Stress model as implemented by CFX proved numerically too unstable to model a swirling flow in a straight or bent pipe.

3) The Reynolds stress model as implemented by CFX does not produce satisfactory results for fully developed flows in rotating or non-rotating straight pipes. There can be several reasons for this (see chapter 5):

-The wall reflection terms are not in the default model and are not programmed in a general way suitable for arbitrary geometries.

-We are bounded to use a wall function whilst other RSM-models produced better results without the use of this function (Jakirlic(1997)).

-CFX never updated the turbulence constants because they did not want users to find different results for identical problems run on different versions of their software. This means that the default constants are not necesarily the correct ones.

4) For a decaying swirl in a straight pipe where we prescribe the axial and tangential velocity profile (obtained from experimental data (Kitoh(1991)) at the inlet, the Reynolds stress model model produces reasonable results in combination with a axi-symmetric simulation (see chapter 6). The inclusion of the wall reflection terms does not improve the results. The mean flow quantities as well as the decay of the swirl intensity are predicted quite well. We were however faced with considerable convergence problems as the model is numerically unstable. It was for instance not possible to prescribe the Reynolds stresses and the dissipation rate at the inlet and in some cases it was necesarry to run transient simulations to ensure convergence. Chen(1992) was able to run steady-state simulations with the inclusion of all the turbulent stress profiles as boundary inlet conditions using different software.

5) The data produced by CFX when simulating the cyclone design is not conform the experi-

mental data. The Reynolds Stress Model generates an extra recirculation cell for this geometry which was not observed by Dirkzwager(1996). There can be several reasons for this (see chapter 7):

-By doing an axisymmetric simulation we are not modelling the a-symmetric features of the flow.

-Instead of modelling the swirl element we are imposing a uniform axial and tangential velocity profile at the inlet.

-We are using a wall function instead of resolving the flow near the wall. Unfortunately we have no choice as CFX implements a wall function automatically for all but the Low-Reynolds $\kappa-\epsilon$ models.

-According to Dirkzwager(1996) the wall region is not constant in the pipe. The slope of the log profile decreases with increasing swirl nuber Ω. The decrease stops at $\Omega > 0.3$ and we have a constant value of the von Karman constant of $\kappa = 0.725$. To simulate this the von Karman constant should be a function of the swirl number. This is not possible in CFX.
-The wall reflection terms are only implemented for one wall so they as are not used for the wall of the swirl element.

-The wall reflection terms are fit for straight walls (as in channel flows) and straight pipe walls. They are however not suitable for bent pipes. This means that the reflection terms are not calculated correctly in the inlet section.

-CFX never updated the turbulence constants because they did not want users to get different results for identical problems run on different versions of their software. This means that the default constants are not necesarily the correct ones.

6) When using the Reynolds stress model we are solving a set of 10 coupled non-linear partial differential equations. This costs a lot of CPU time and gives considerable numerical problems. These problems are probably due to a badly conditioned matrix (see Appendix A).

7) Axi-symmetric simulations using the Reynolds stress model on swirling straight pipe flows are possible when having prior knowledge of the velocity profiles at the inlet. The mean flow quantities are predicted reasonably well. For more difficult geometries and without prior knowledge of the inlet conditions the velocity profiles are not predicted correctly. Therefore it is not recommended to use this numerical tool in this way for designing purposes of cyclones. It would be interesting to see what different commercial CFD software would predict for the Dirkzwager(1996) cyclone as CFX-4.2 has limitations concerning the use of the wall reflection terms and the wall function. A three-dimensional time-dependant simulation of the Dirkzwager(1996) cyclone (the swirl element with the guide vanes should also be modelled) should give more insight in the applicability of RANS simulations using the Reynolds stress model for swirling flows in complex geometries.

Appendix A

Matrix Conditioning

This Appendix aims at explaining the effect of transient simulations on the condition of the matrix which is solved during the simulations. We will use the 1-D advection/diffusion equation as an example, which is also a transport equation. First we take a look at the time-independent equation:

$$u\frac{\partial T}{\partial x} = \Gamma\frac{\partial^2 T}{\partial x^2} \tag{A.1}$$

When we discretisize eq. A.1 using upwind for the advection term and central for the diffusion term:

$$u\frac{T_i - T_{i-1}}{\Delta x} = \Gamma\frac{T_{i-1} - 2T_i + T_{i+1}}{\Delta x^2} \tag{A.2}$$

Rewriting the equation into a form which we can fit into a tri-diagonal matrix:

$$A_i T_{i-1} - B_i T_i + C_i T_{i+1} = -q_i, i = 1, 2....N - 1 \tag{A.3}$$

gives the following coefficients:

$$A_i = \frac{u}{\Delta x} + \frac{\Gamma}{\Delta x^2}, B_i = -\frac{u}{\Delta x} - 2\frac{\Gamma}{\Delta x^2}, C_i = \frac{\Gamma}{\Delta x^2} \tag{A.4}$$

Now we will do the same for the instationary 1-D advection/diffusion equation:

$$\frac{\partial T}{\partial t} + u\frac{\partial T}{\partial x} = \Gamma\frac{\partial^2 T}{\partial x^2} \tag{A.5}$$

$$\frac{T_i^{n+1} - T_i^n}{\Delta t} + u\frac{T_i^{n+1} - T_{i-1}^{n+1}}{\Delta x} = \Gamma\frac{T_{i-1}^{n+1} - 2T_i^{n+1} + T_{i+1}^{n+1}}{\Delta x^2} \tag{A.6}$$

The spatial discretization is the same as in eq. A.2 and we used a Euler backwards scheme for the temporal discretization. Now the coefficients are:

$$A_i = \frac{u\Delta t}{\Delta x} + \frac{\Gamma \Delta t}{\Delta x^2}, B_i = 1 + \frac{u\Delta t}{\Delta x} + 2\frac{\Gamma \Delta t}{\Delta x^2}, C_i = \frac{\Gamma \Delta t}{\Delta x^2} \tag{A.7}$$

When we look at the coefficient B_i for the transient case, we see it has an extra term of order unity compared to B_i for the stationary case. Because the B_i coefficients are placed on the main diagonal this results in a better conditioned matrix. This is advantagear for iterative solvers.

Appendix B

References

Kitoh, O. (1971) *Experimental study of turbulent swirling flow in a straight pipe.* J.Fluid Mech., Vol. 225, pp 445-479.

Dirkzwager, M. (1996) *A New Axial Cyclone Design for Flui-Fluid Separation.* Ph.D. Thesis. T.U.Delft.

Eggels, J.G.M. (1994) *Direct and Large Eddy Simulation of Turbulent Flow in a Cylindrical Pipe Geometry.* Ph.D. Thesis. T.U.Delft.

Chen, Q. (1992) *Numerical Prediction of Turbulent Swirling Flow in a Straight Pipe.* Internal report MEAH-104. T.U.Delft.

Gibson, M.M. and Launder, B.E. (1978) *Ground effects on pressure fluctuations in the atmospheric boundary layer.* J.Fluid Mech., Vol. 86, pp 491.

Faler, J.H. and Leibovich S. (1978) *An experimental map of the internal structure of a vortex breakdown.* J.Fluid Mech., Vol. 86, pp 313-335.

Nieuwstadt, F.T.M. (1998) *Turbulentie.* Epsilon Uitgaven, Utrecht.

Wilkes, N.S. and Clarke, D.S.(1987) *Turbulent flow predictions using Algebraic stress models.* AERE-R 12694.

Clarke, D.S. and Wilkes, N.S. (1989) *The calculation of turbulent flows in complex geometries using a Differential Stress Model.* AERE-R 13428.

Rotta, J.C.(1951) *Statistische Theorie nichthomogener Turbulenz.* Z.Phys., Vol. 129,pp 547

Reich, G. (1988)*Stromung und Warmteubertragung in einem axial rotierenden Rohr.* Ph.D. Thesis (D17), Technische Hochschule Darmstadt, Germany.

Nishibori, K., Kikuyama, K. and Muakami, M.(1987) *Laminariazation of turbulent flow in the inlet region of an axially rotating pipe.* Int.J.JSME, No.260, Vol. 30, pp 255-262.

Kikuyama, K., Muakami, M., Nishibori, K. and Maeda, K. (1983a) *Flow in an axially rotating pipe.* Bull. of the JSME, No 214, Vol. 26, pp 506-513.

Pericleous, K.A. and Rhodes, N.(1986) *The hydrocyclone classifier - A numerical approach.* Int.J Min.Proc., 17 : 23.

Launder, B.E., Priddin C.H. and Sharma, B.I.(1977) *The calculation of turbulent boundary layers on spining and curved surfaces.* ASME, J. of Fluids Eng., Vol. 99, pp 231-239.

CFX. (1997) CFX-4.2 Solver Manual.

Appendix C

Acknowledgement

The author is grateful to Prof.Dr.Ir.F.T.M. Nieuwstadt, Prof.Dr.K. Hanjalic, Dr. R. Delfos and Dr.Ir. M. Pourquie for their assistance during this study.